



# Seismic and Tsunami Hazard Potential of the Negros-Sulu Megathrust, Philippines

Lyndon P. Nawanao Jr.<sup>1</sup>, Noelynna T. Ramos<sup>1</sup>, Toshitaka Baba<sup>2</sup>, Naotaka Chikasada<sup>3</sup>, and Kenji Satake<sup>4,5</sup>

- <sup>1</sup> National Institute of Geological Sciences, University of the Philippines Diliman, Quezon City, 1101, Philippines
- <sup>2</sup> Graduate School of Science and Technology, Tokushima University, Tokushima, Japan
- <sup>3</sup> National Research Institute for Earth Science and Disaster Resilience, Tsukuba, Japan
- <sup>4</sup> Earthquake Research Institute, The University of Tokyo, Tokyo, Japan
- <sup>5</sup> Department of Earth Sciences, National Central University, Taoyuan, Taiwan

Correspondence to: Lyndon P. Nawanao Jr. (lyndon.nawanao@nigs.upd.edu.ph)

10 Co-correspondence to: Noelynna T. Ramos (noelynna.ramos@up.edu.ph)

## **Short Summary.**

The scarcity of information on the Negros–Sulu megathrust impedes reliable seismic and tsunami hazard assessments. Here, we estimated 18 megathrust rupture scenarios based on available data and modeled tsunami propagations to identify highly exposed coastal areas surrounding the Sulu Sea. The generated rupture parameters, maximum wave heights, flow velocity, and minimum arrival times provide a significant basis for exploring prehistoric tsunami deposits and informing risk mitigation policies.

Abstract. The Negros–Sulu megathrust poses an imminent threat to coastal communities surrounding the Sulu Sea, but with limited information on past tsunamis, megathrust geometry, and locked segments, robust seismic and tsunami hazard assessments are hindered. To identify highly exposed coastal areas amid this knowledge gap, we estimated the Negros–Sulu megathrust source parameters using a structural-based segmentation and scaling-relation approach for tsunami modeling. A total of 18 sets of source parameters from six segments and three dip angle scenarios were considered with moment magnitude and average slip of Mw 8.0–8.9 and 1.68–6.23 m, respectively. Tsunami simulations were modeled in JAGURS, accounting for nonlinear shallow water equations, horizontal and vertical seafloor displacements, and Boussinesq dispersion effects. Coastal regions directly facing the segments have the highest exposures with <2 min arrival times, highlighting the major control of wave directivity and the need for rapid evacuation strategies. The Negros Trench generates up to 6 m wave height and 7 m/s flow velocity, while the Sulu Trench up to 8 m and 6 m/s. Coastal areas with ≥2 m wave heights typically exhibit a concave morphology with a nearshore width interquartile range of 2–4.5 km. At wider nearshore width (>20 km), wave dissipation results in lower wave heights (<2 m) that underscore accurate nearshore bathymetry in tsunami modeling. This study provides exposure maps of the maximum wave height, flow velocity, and minimum arrival times from rupture scenarios for searching paleotsunami deposits and most importantly for policymakers, local government, and coastal communities to mitigate tsunami hazard risk.

35 **Keywords**: Negros–Sulu subduction zone, Sulu Sea, tsunami modeling, tsunami hazard exposure

## 1 Introduction

Tsunamis brought about by megathrust ruptures are infrequent but have led to the most damaging coastal disasters in recorded history. The Mw 7.8–8.2 1923 Taisho Kanto (Satake, 2023), 9.5 Mw 1960 Valvidia (Duke, 1960), 9.2 Mw 1964 Great Alaska (Brocher et al., 2014), 9.2 Mw 2004 Indian Ocean (Athukorala & Resosudarmo, 2005), and 9.1 Mw 2011 Tohoku-Oki (Kajitani et al., 2013; Suppasri et al., 2012) events led to accumulated casualties of more than 380,000 and billions (USD) worth of damage. In the Philippines, Bautista et al. (2012) collated 41 positive tsunamigenic earthquake events from 1589 to 2012, primarily based on eyewitness accounts and previous reports. Of the 41 events (**Figure 1a**), 20 can be directly



50

55



linked to subduction zones, and three subduction-related events have a magnitude of at least 8.0: The 1918 Ms 8.0 and 1976 Mw 8.1 events along the Cotabato Trench with up to 8 m and 9 m maximum tsunami wave height, respectively, and the 1946 Ms 8.2 event along the Negros Trench but with a lower maximum tsunami wave of 2 m. The 1976 Mw 8.1 is the most damaging historical tsunami event in the Philippines, characterized by a shallow rupture with a 25 km depth leading to estimated casualties of 3,000–8,000 (Acharya, 1978; Badillo & Astilla, 1978; Stratta et al., 1977). A washover deposit (766–675 cal BP) was also discovered along the coasts of Zamboanga del Sur facing the Cotabato Trench, suggesting an extreme wave event (tsunami or storm surge) prior to the 1976 earthquake and tsunami (Claro et al., 2021).

One of the primary goals when inferring future megathrust ruptures is to establish seismic gaps, and coupling models with slip deficits are used to derive these locked segments from geodetic measurements (e.g., Chlieh et al., 2008; Métois et al., 2013, 2016; Michel et al., 2019; Moreno et al., 2010; Ozawa et al., 2012). However, with the current temporal limitation of geodetic records compared with the hundred-to-thousand-year recurrence of megathrust earthquakes, uncertainty remains regarding the possible extent of ruptures.

Coupling models have been constrained in the Manila, East Luzon, and Philippine Trench as well as along the Philippine Fault Zone (PFZ) (Galgana et al., 2007; Hsu et al., 2012, 2016) as GPS networks are dense in these regions. On the other hand, a sparse GPS network along the Negros–Sulu Trench inhibits identifying locked segments with slip deficits that may rupture. The current Slab 2.0 of global subduction zone geometry (Hayes et al., 2018) includes all trenches in the Philippines except the Negros–Sulu Trench, and while previous studies have provided tomography profiles of the Negros Trench (Fan et al., 2017; Fan & Zhao, 2019), the geometry of the Negros–Sulu megathrust remains uncertain.

Although earlier source estimation and tsunami modeling exist in this active margin (Nurashid et al., 2013; Okal et al., 2011; Pedersen et al., 2011; Salcedo & Hara, 2011; Zhao & Niu, 2022), the uncertainties of the slab geometry were not accounted for, as well as updated scaling equations more suitable for megathrust ruptures, nonlinear effects, and Boussinesq dispersion. To fill these gaps and provide crucial information on the tsunami wave characteristics, this study estimated the megathrust earthquake source parameters in the Negros and Sulu subduction zones using a structural-based segmentation and scaling-relation approach. We produced three slab dip scenarios and used the estimated source parameters to model tsunamis and identify potentially exposed coastal areas across the coastal areas surrounding the Sulu Sea.

#### 2 Seismotectonic Setting

The amalgamation of different terranes in the Philippine Mobile Belt is a consequence of the complex interaction among the Pacific, Philippine Sea, Eurasia, and Indo–Pacific plates, leading to its present configuration marked by oppositely dipping subduction zones and the PFZ across the archipelago (Aurelio, 2008; Aurelio et al., 2013; Hilde et al., 1977; Holloway & Hall, 1996; Yumul et al., 2003, 2008; Zahirovic et al., 2014). These subduction zones include the East Luzon Trough, Philippine, Manila, Negros–Sulu, and Cotabato trenches that can potentially generate great to epic (M >8) megathrust earthquakes (e.g., Li et al., 2016; Qiu et al., 2019; Ramos et al., 2017; Wu & Huang, 2009). Peñarubia et al. (2020) evaluated an empirical Gutenberg–Richter (GR) magnitude—frequency distribution (MFD) in these subduction zones with b-values ranging from 0.691 to 1.724, based on the declustered seismicity catalog from the International Seismological Centre (ISC) and the Philippine Institute of Volcanology and Seismology (PHIVOLCS), where <1.0 are associated with a higher proportion of large earthquakes and stress accumulation (Nishikawa & Ide, 2014). In the study, the evaluated number of declustered seismicity in all trench segments was less than 300, with the majority of the segments having <50 earthquakes (Peñarubia et al., 2020). In the Negros and Sulu subduction zones, only 7 and 21 earthquakes, respectively, were used to evaluate the GR MFD, with resulting b-values of 1.084 for Negros and 0.797 for Sulu. With longer and denser seismicity records, constraints on the GR MFD in this region will further improve.

Inland GPS networks in the Philippines (Galgana et al., 2007; Hsu et al., 2016; Kreemer et al., 2014; Rangin et al., 1999) are mostly distributed in Luzon and eastern Philippines, revealing a west-northwest motion (**Figure 1a**), while sparse GPS data in the southwestern Philippines show a south—southwest direction. The oceanic plates subducting beneath the five subduction zones have a crustal thickness ranging from 7 to 15 km (**Figure 1b**), where relatively thicker crusts (>15 km) are linked to the island arcs across the Philippine Archipelago (Laske et al., 2013). PHILCRUST 3.0 provides a higher resolution inland crustal thickness varied by different island growth rates and terranes (Parcutela et al., 2020). Based on the global dataset from Straume et al. (2019), the majority of marginal seas and active margins in the Philippines are characterized by ≥1 km





- thick overlying sediments (Figure 1c), except in the Philippine Sea. The Sulu Sea is particularly marked by high sediment thickness of up to 6 km. Estimates on the gravity variations in the Philippines from Balmino et al. (2012) show distinct high Bouguer anomalies (>300 mGal) of the subducting oceanic basins where the trench marks the boundary of the active margin and island arcs with relatively lower (<300 mGal) Bouguer anomaly signatures (Figure 1d). The NW Sulu sub-basin, with the thickest sediments, has a lower Bouguer anomaly than the SE Sulu sub-basin. Past GPS campaigns estimated convergence
- rates of <60 mm/yr along the Negros-Sulu subduction zone (Rangin et al., 1999; Simons et al., 1999).





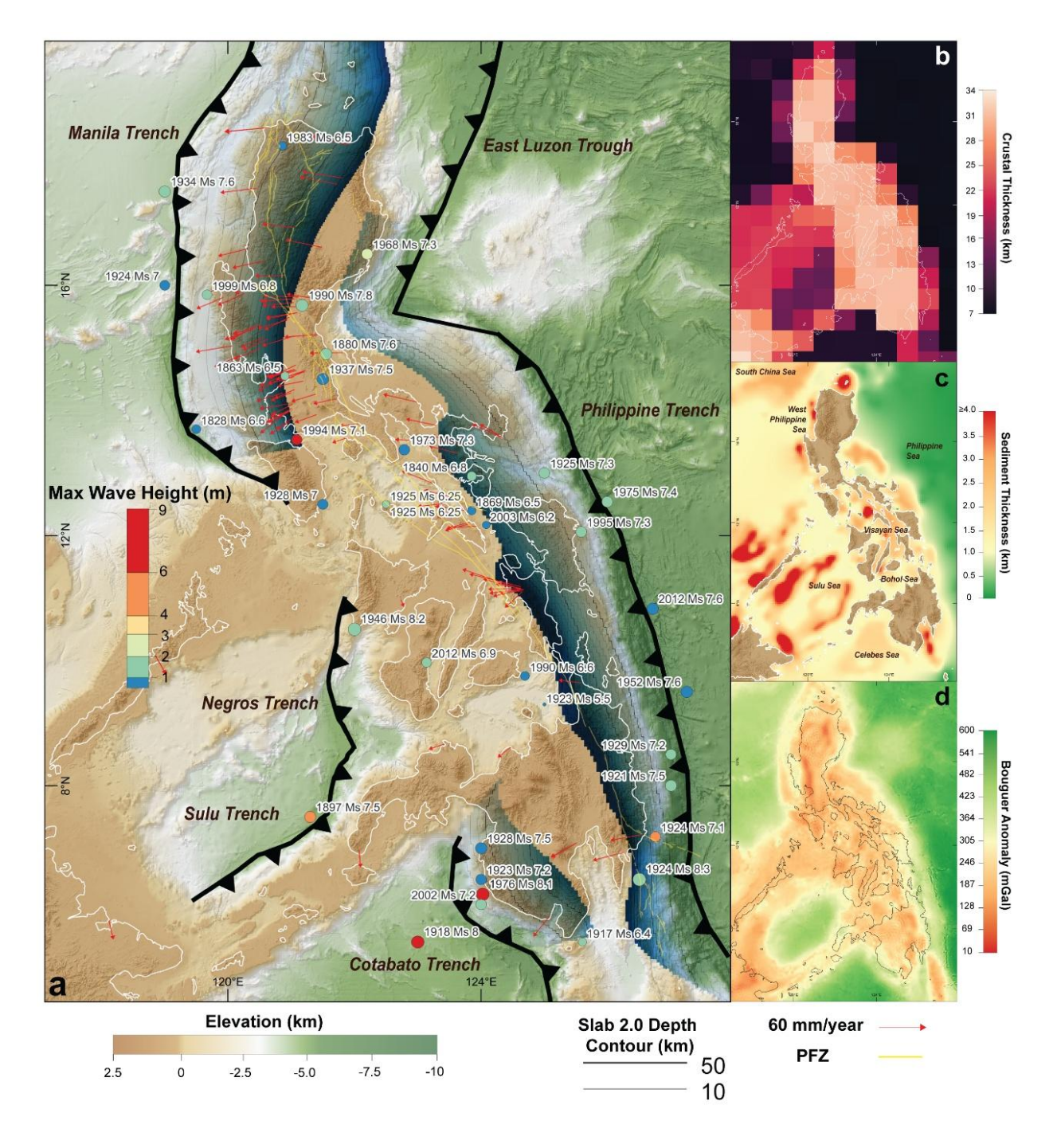


Figure 1. Philippine tectonic setting. (a) Positive tsunamigenic earthquakes and reported maximum wave heights since 1589 (Bautista et al., 2012). The trace of the Philippine Fault Zone (PFZ) was adapted from PHIVOLCS. Depth contours of the Slab 2.0 model from Hayes et al. (2018). Arrows indicate the velocity vectors from inland GPS networks (Kreemer et al., 2014). Bathymetry and topography data from the 2024 General Bathymetric Chart of the Oceans (GEBCO) (GEBCO Compilation Group, 2024). (b) Crustal





thickness (Laske et al., 2013), (c) sediment thickness (Straume et al., 2019), and (d) Bouguer anomaly (Balmino et al., 2012) across the archipelago.

#### 105 3 Methodology

110

115

### 3.1 Constraining Megathrust Fault Parameters

Simplified rectangular fault models were adapted for the megathrust with parameters length (km), width (km), strike (°), dip angle (°), depth from the seafloor (km), rake (°), and slip amount (m). We utilized a structural-based segmentation in which the megathrust fault length is derived from the orientation variations of the frontal wedge (i.e., Nawanao & Ramos, 2023), and the width and bottom depth are limited by the seismogenic zone. Insights from previous seismic tomography profiles of Fan et al. (2017) and Fan and Zhao (2019) on the geometry of the subducting slab reveal tapering of high p-wave velocity in the northern Negros Trench segment west of Panay Island, which provides limiting constraints on the length of the northern Negros Trench segment. Steepening of the subducting slab was also observed in the seismic tomography profiles around 100 km depth, although this is well beyond global seismogenic zones. Best-fit estimates on the slab dip of the shallow portion of the subducting slab from the tomography profiles within a 50 km range from 9° to 30°. Focal mechanism solutions of reverse-oblique rake values ranging from 10° to 170° collated by the ISC from 1977 to 2023 (Bondár et al., 2015; Di Giacomo et al., 2015, 2018; Storchak et al., 2013, 2015) also show a wide distribution of dip angles ranging from 9° to 90° (Figure 2). To account for this uncertainty of the slab dip, we used three dip angles for all source parameters at 10°, 20°, and

120 Based on the interquartile range (1.5IQR) of 207 reverse-oblique earthquakes (Figure 2), a threshold depth of 50 km was set as the limit of the seismogenic zone. The 50 km depth also serves as the limiting factor in calculating the width of the seismogenic zone using the sine function, given the three dip angles (Figure 3). A saturation width of 196 km was set as the maximum, adapting Allen and Hayes (2017), and we assumed a rake of 90° of purely thrust motion. A shallow blind rupture is assumed for all scenarios with a top depth of 5 km. The area (S) of the fault plane is used as input in the linear rupture-125 scaling equations (Eqs. 1-3) of Allen and Hayes (2017) to account for both length and width of the megathrust in estimating the Mw, and the average  $(D_{ave})$  and maximum  $(D_{max})$  slip amount (m):

$$\log_{10} S^1 = -3.63 + 0.96 \times M_w^2 \tag{1}$$

$$\log_{10} D_{ave}^{3} = -5.05 + 0.66 \times M_{w}^{4} \tag{2}$$

log<sub>10</sub> 
$$D_{max}^{5} = -4.94 + 0.71 \times M_{w}^{6}$$
 (3)

Standard deviation ( $\sigma$ ) =  $\pm 0.255$ 

 $^{2}\sigma = \pm 0.266$ 

 $^{3}\sigma = \pm 0.209$ 

 $^{4}\sigma = \pm 0.315$ 

 $^{5}\sigma = \pm 0.179$ 

135  $^{6}\sigma = \pm 0.254$ 





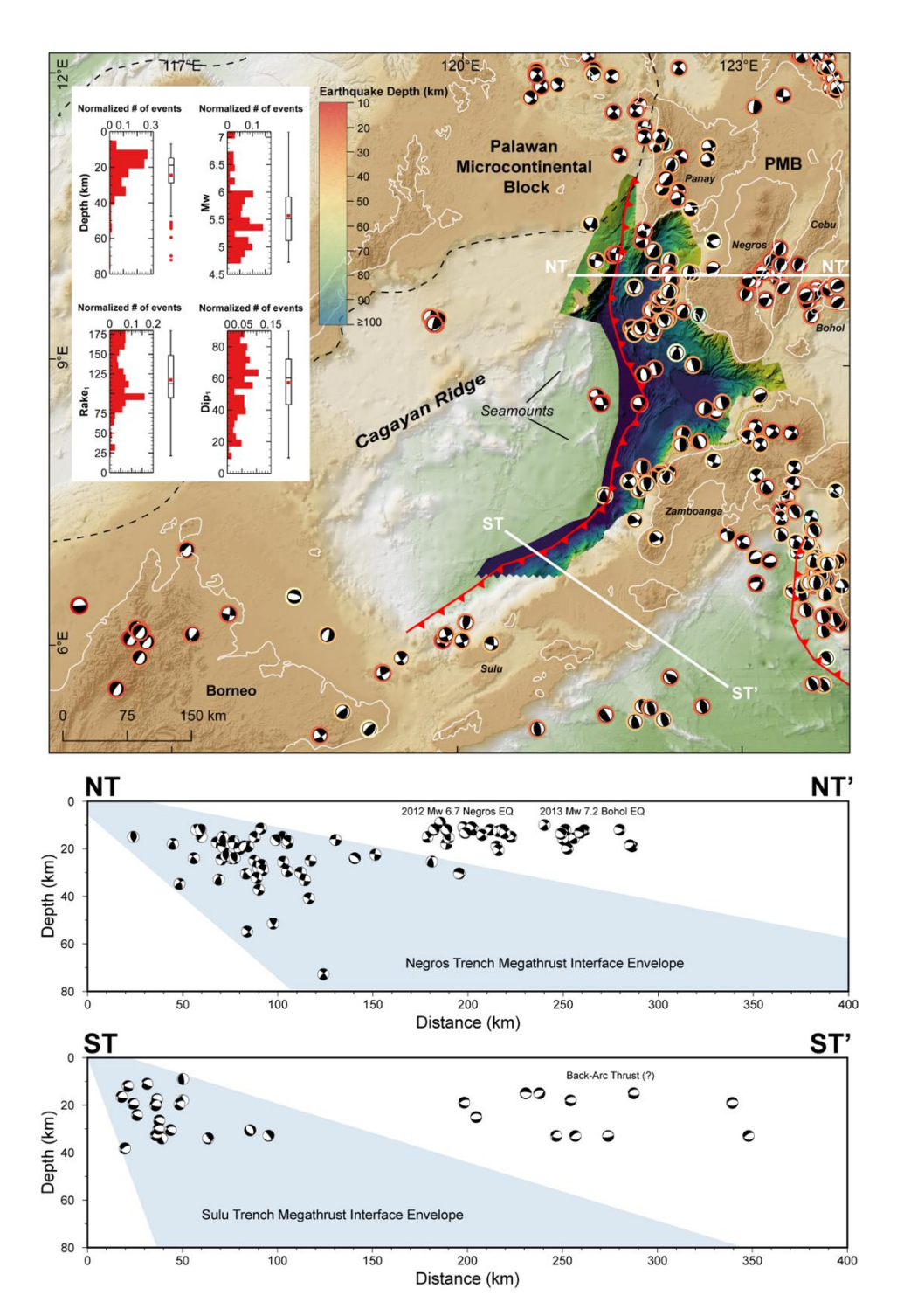


Figure 2. Reverse-oblique focal mechanism solutions (1977–2023) of earthquakes along the Negros-Sulu subduction zone collated by the International Seismological Centre (ISC) (Bondár et al., 2015; Di Giacomo et al., 2015, 2018; Storchak et al., 2013, 2015).





Earthquakes in the cross-sectional profiles (NT-NT' and ST-ST') are within 80 km depth and 200 km distance from each side of the profile. The possible interface of the megathrust fault plane is marked in the light blue zone.

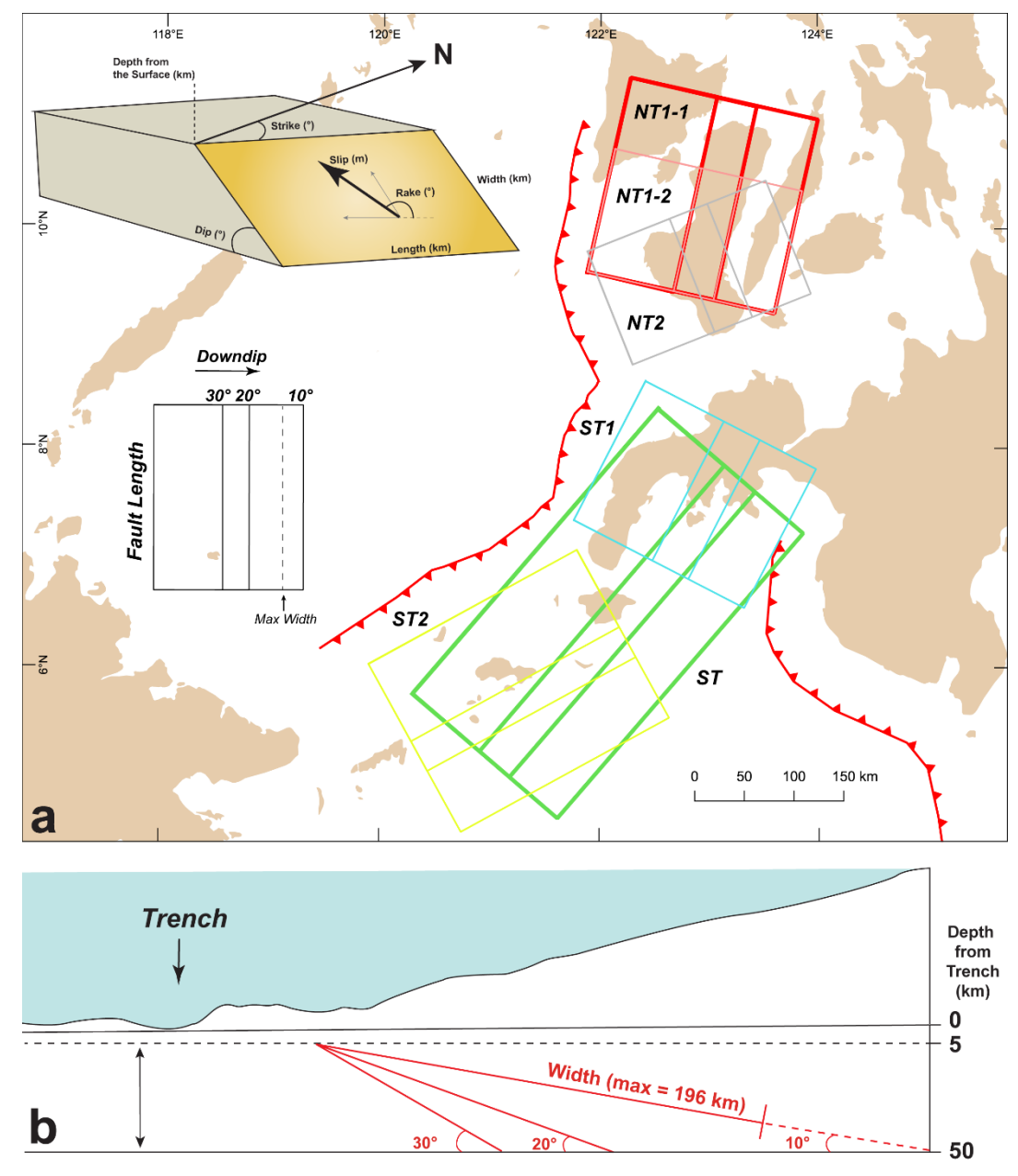


Figure 3. Megathrust fault parameterization of Negros-Sulu Trench segments. (a) A total of 18 sets of megathrust fault parameters were utilized for the tsunami modeling based on six segments and three dip angle scenarios. (b) Cross-section schematic diagram of the megathrust plane, where the width saturates at 196 km and is calculated using sine function.



160



## 3.2 Tsunami Modeling

We utilized the 15 arcsec-resolution 2024 General Bathymetric Chart of the Oceans (GEBCO) bathymetry data (GEBCO Compilation Group, 2024) as input for the tsunami simulation. To have a higher elevation accuracy of the topography, we resampled the interferometric synthetic aperture radar (IFSAR)-derived 5 m-resolution digital terrain model (DTM) (±1 m vertical accuracy) from the National Mapping and Resource Information Authority (NAMRIA) to 15 arcsec and merged with the GEBCO bathymetry data. The resulting IFSAR DTM-bathymetry raster served as the input depth in computing the initial seafloor and seawater displacement for tsunami modeling. As the entire coastal areas surrounding the Sulu Sea were considered for tsunami simulations, high-resolution subgrids for inundation models were not performed due to restrictions in computational capacity and processing time.

The elastic deformation from the finite rectangular fault source is analytically solved through Green's function, assuming a homogeneous isotropic elastic half-space (Okada, 1985) and utilizing the average slip from the scaling equation. The tsunami wave propagation is modeled using two-dimensional nonlinear shallow water equations through the finite difference method (FDM) in a staggered grid deployed in the JAGURS numerical code (Baba et al., 2015, 2017). In JAGURS, both the initial vertical and horizontal seafloor displacement and Boussinesq dispersion effects are accounted for in the tsunami propagation. The modeling assumes a uniform surface roughness (Manning's coefficient = 0.025 s m<sup>-1/3</sup>), and we set a time step ( $\Delta t$ ) of 0.5 s to maintain stability conditions based on the lowest depth (d), bathymetry resolution ( $\Delta x$ ), and acceleration due to gravity (g) in Eq. 4 (Satake, 2002):

$$\Delta t \le \frac{\Delta x}{\sqrt{2gd}} \tag{4}$$

The tsunami wave propagation time was set to 4 h, and 34 synthetic tide gauge stations (TGS) (**Figure 4** and **Table S1**) were positioned across the coastal areas surrounding the Sulu Sea. The coastal areas surrounding the Negros–Sulu Trench are subdivided into 16 regions: I, Visayan Sea; II, Mindoro; III, Coron–Cuyo; IV, West Panay; V, Panay Gulf; VI, Sipalay–Bayawan; VII, Tañon–Cebu Strait; VIII, Bohol Sea; IX, Leyte Gulf; X, Palawan; XI, Cagayancillo; XII, Sindangan–Labason; XIII, Siocon–Sibuco; XIV, Basilan–Sulu; XV, Moro Gulf; and XVI, northeast Borneo. To represent the minimum arrival time, maximum wave height, and flow velocity across the coastlines, 6,879 sampling points were set at 10 km intervals, each with a radius of 5 km.





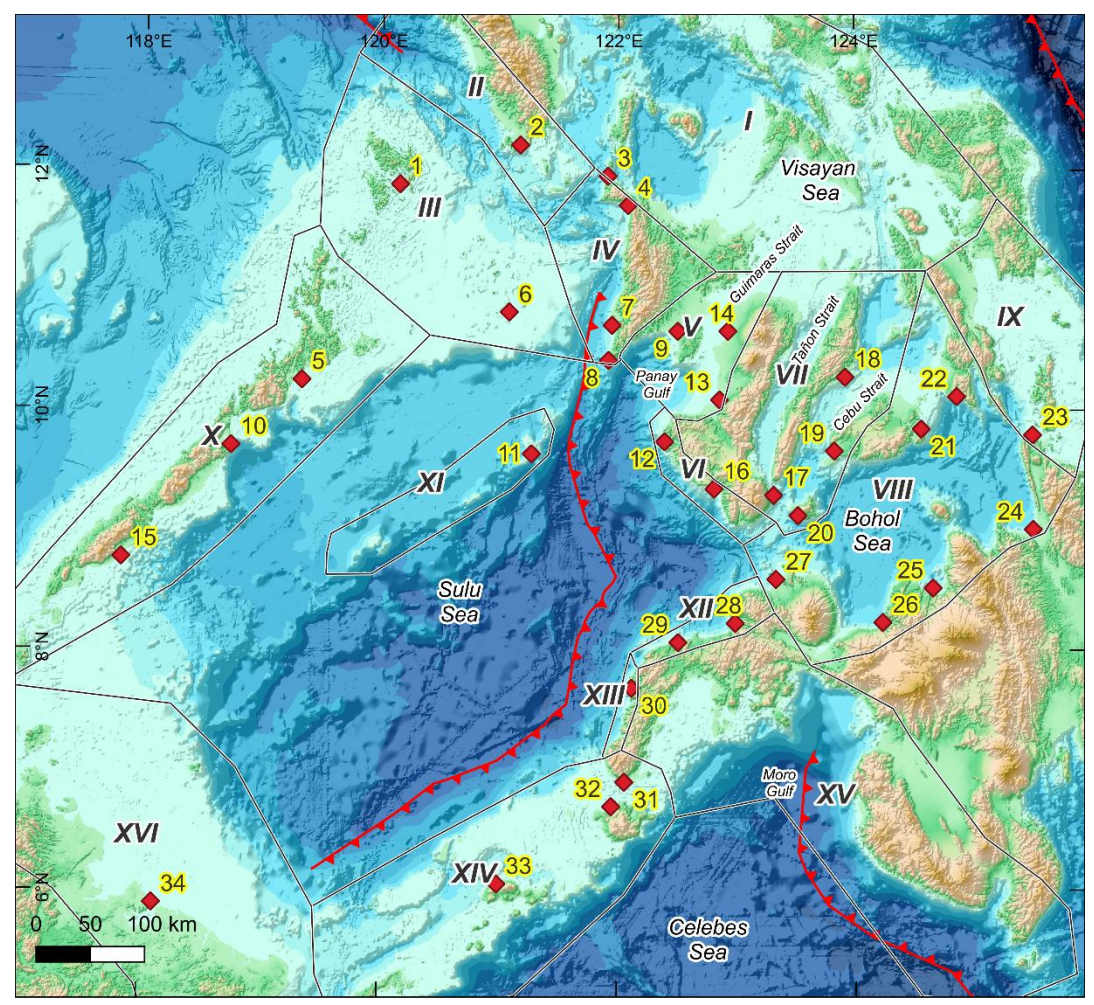


Figure 4. The 16 coastal regions surrounding the Negros-Sulu subduction zone and the 34 synthetic tide gauge stations (TGS). I, Visayan Sea; II, Mindoro; III, Coron-Cuyo; IV, West Panay; V, Panay Gulf; VI, Sipalay-Bayawan; VII, Tañon-Cebu Strait; VIII, Bohol Sea; IX, Leyte Gulf; X, Palawan; XI, Cagayancillo; XII, Sindangan-Labason; XIII, Siocon-Sibuco; XIV, Basilan-Sulu; XV, Moro Gulf; XVI, northeast Borneo. Basemap from GEBCO Compilation Group (2024).

#### 4 Results

175

180

185

## 4.1 Megathrust Source Parameters

The Negros–Sulu Trench was divided into four segments, namely, NT1, NT2, ST1, and ST2. The NT1 and NT2 are marked by north-northeast and north-northwest orientations, respectively, while the ST1 and ST2 by north-northeast and northeast, respectively (**Figure 3a**). Due to the uncertainty of the northern extent of NT1 where p-wave velocity profiles of Fan et al. (2017) and Fan and Zhao (2019) indicate tapering of the slab northward, we included longer (NT1-1) and shorter (NT1-2) rupture lengths for NT1. For the Sulu Trench, an additional longer segment (ST) that combines ST1 and ST2 is also proposed due to their similar northeast trend. This segmentation results in six subfaults, i.e., NT1-1, NT1-2, NT2, ST, ST1, ST2. Utilizing three dip angles 10°, 20°, and 30° to represent gently- to steeply-dipping megathrust scenarios, a total of 18 sets of source parameters were constrained for elastic dislocation and tsunami modeling, with the ST (379 km) and NT1-1 (201





km) having the longest lengths (**Table 1**). Based on the sine function of the 5 km top depth and 50 km lower depth limit, the width of the segments with dip angles 10°, 20°, and 30° corresponds to 196 km (maximum width limit), 132 km, and 90 km, respectively. Estimates of the moment magnitude from scaling equations range from Mw 8.0 to 8.9, where the ST segment with the largest fault length has the largest magnitude. These earthquake magnitudes correspond to average and maximum slip ranges of 1.68–6.23 m and 5.44–22.26 m, respectively.

#### 4.2 Tsunami Models

210

215

235

Figure 5 and S1–S5 (in the Supplementary Material) show the representative wave propagation snapshots from rupture scenarios of six segments (NT1-1, NT1-2, NT2, ST, ST1, ST2) based on the 20° slab dip. The initial wave propagation from all ruptures is characterized by strong east—west and northwest—southeast wave crests in the Negros and Sulu Trench, respectively. Short-period wave dispersion and interferences are also prevalent as waves propagate toward shallower depths. In I, III, VII, VIII, and IX, the combined effects of dispersion, diffraction, and refraction caused significant deformation of wave crests as they propagated toward the coasts.

Coastal islands in direct proximity have <2-min arrival time, including V and VI for Negros Trench segments and XII, XIII, and XIV for Sulu Trench segments. Arrival times from Negros Trench segments in XI, XII, XIII, and northeast of X were about 10 min, 15 min, 30 min, and 45 min, respectively. As the initial wave approaches shallow depths, speed significantly drops as indicated by the compression of arrival time contours (**Figure 6**). For instance, the first wave arrives in the southwest of X about 1 h after the initial displacement, while about 2 h in XVI. The effects of wave refraction, diffraction, and interference are also apparent in the deformed arrival time contours in the majority of coastal regions.

For ST and ST1 segments, the initial wave arrives in VI, XI, IV, and III by 10 min, 20 min, 25 min, and 45 min, respectively. For ST2 segments, arrival times are around 30 min in VI and XI, while around 35 min, 45 min, and 1 hr in XVI, V, and III, respectively. Tsunami waves from Sulu Trench segments can also pass through the XIV and propagate across the Celebes Sea, arriving in XV at about 10 min (**Figure 6**).

Waveforms from 34 synthetic tide gauge stations (**Figure 7–Figure** 8 and **S6–S7**) also indicate the arrival as the first crest or trough. Relatively long-period waves are apparent in TGS 1 Coron, 2 Pandarochan Bay, 13 Himamaylan, 14 Bacolod, and 18 Cebu, while the majority are dominated by short-period waves due to nonlinear and dispersion effects. Tsunami waves from all segments did not propagate in TGS 22 Surigao City within the 4 h simulation. In TGS 33 Jolo, dissipation also led to no tsunami waveforms from NT and ST1, while the ST and ST2 ruptures caused coastal uplift.

The maximum wave height and flow velocity from six segments are shown in **Figure 9** (**Figs. S8–S9**) and **Figure 10** (**Figs. S10–S11**), respectively. The highest wave heights (>2 m) are observed in coastal areas parallel to the rupture segments, as also indicated in six tide gauge stations (13, 16, 28, 29, 30, 32). For NT1, tsunami waves reached up to 4–5 m in VI. For the NT2 segment, tsunami waves of up to 4 m are localized in VI. For ST and ST1 segments, the highest wave heights are located in XII (8 m) and XIII (5–7 m). Tsunami waves from ST segments propagate across the Celebes Sea, reaching 3–7 m in XV.

Coastal areas on the rear side and parallel to the trench segment also have relatively high tsunami waves. Negros Trench segments produced up to 2–3 m of tsunami wave heights in III and 1–2 m in XI and northeast of X. Sulu Trench segments also produced up to 3–4 m in X and up to 1–2 m in XI and III. The majority of the central Philippines (I, VII, VIII, IX), as well as in XVI, have wave heights of <1 m, except in some embayments and narrow channels where amplifications can reach 1–2 m.

The maximum tsunami wave height and flow velocity are coupled, i.e., coastal areas with the highest tsunami waves also have the highest flow velocity. For Negros Trench segments, the coastal areas with high tsunami waves in VI correspond to flow velocities of 3–7 m/s, while reaching up to 3 m/s in III. For Sulu Trench segments, coastal areas in XII, XIII, XIV, and XV with the highest tsunami waves are exposed to a flow velocity of 3–6 m/s. In coastal areas of northeast Palawan, the flow velocity reached 3–4 m/s. The majority of coastal areas with up to 1 m tsunami wave height correspond to a maximum velocity of <1 m/s.

**Table 2** summarizes the maximum, minimum, and average differences of the maximum tsunami wave height and flow velocity from megathrust segments at 10° dip compared to 20° and 30°. A shallow-dipping megathrust tends to produce the largest earthquakes (Bletery et al., 2016; Schellart & Rawlinson, 2013), hence the use of the 10°-dip rupture parameter as a reference. This tendency is highlighted by the positive average and maximum differences among parameters. However, in certain regions, steeper initial seawater displacement from rupture parameters with 20° and 30° dip angles produced waveforms





that preferentially led to higher maximum wave height and flow velocity as represented by the negative minimum differences. The spatial distribution of the maximum wave height and wave velocity differences among parameters is indicated in **Figure 11** and **S12–S14**.

For Negros Trench segments, the range of maximum difference is 0.934–2.507 m and 0.968–1.811 m/s for maximum wave height and flow velocity, respectively, while the average differences are 0.008–0.104 m and 0.002–0.071 m/s. The minimum differences range from -0.529 to -1.141 m (maximum wave height) and -1.099 to -2.140 m/s (maximum flow velocity). For Sulu Trench segments, the differences are higher than those from Negros Trench segments, with a range of 2.289–5.622 m (maximum wave height) and 2.369–4.509 m/s (maximum flow velocity) for the maximum, 0.014–0.116 m and 0.003–0.017 m/s for the average, and -0.481 to -1.890 m and -1.020 to -2.164 m/s for the minimum.





Segment	Strike (°)	Corner Lon.	Corner Lat. (°)	Length (km)	Rake (°)	Top Depth (km)	Dip	Width (km)	Fault Plane Area (km²)	Mw	Average Slip (m)	Maximum Slip (m)
							10	196	39455	9.8	4.03	13.93
NT1-1	12.6	121.88	9.616	201	06	S	20	132	26485	8.4	3.07	10.37
							30	06	18117	8.2	2.36	7.83
							10	196	24912	8.4	2.94	9.91
NT1-2	12.9	121.88	9.616	127	06	S	20	132	16723	8.2	2.23	7.38
							30	06	11439	8.0	1.72	5.57
							10	196	24108	8.4	2.87	89.6
NT2	338	122.3	8.773	123	06	5	20	132	16183	8.2	2.18	7.21
							30	06	11070	8.0	1.68	5.44
							10	196	74362	8.9	6.23	22.26
ST	40.6	120.3	5.77	379	06	S	20	132	49918	8.7	4.74	16.57
							30	06	34146	8.5	3.65	12.52
							10	196	30694	8.5	3.39	11.57
ST1	27.2	121.77	7.355	157	06	S	20	132	20604	8.3	2.58	8.61
							30	06	14094	8.1	1.99	6.50
							10	196	46883	8.7	4.54	15.82
ST2	61	119.9	6.032	239	06	5	20	132	31472	8.5	3.45	11.78
							30	06	21528	8.3	2.66	8.90

Table 1. Negros-Sulu megathrust fault parameters of the six segments and three dip angle scenarios based on the scaling equations of Allen and Hayes (2017).





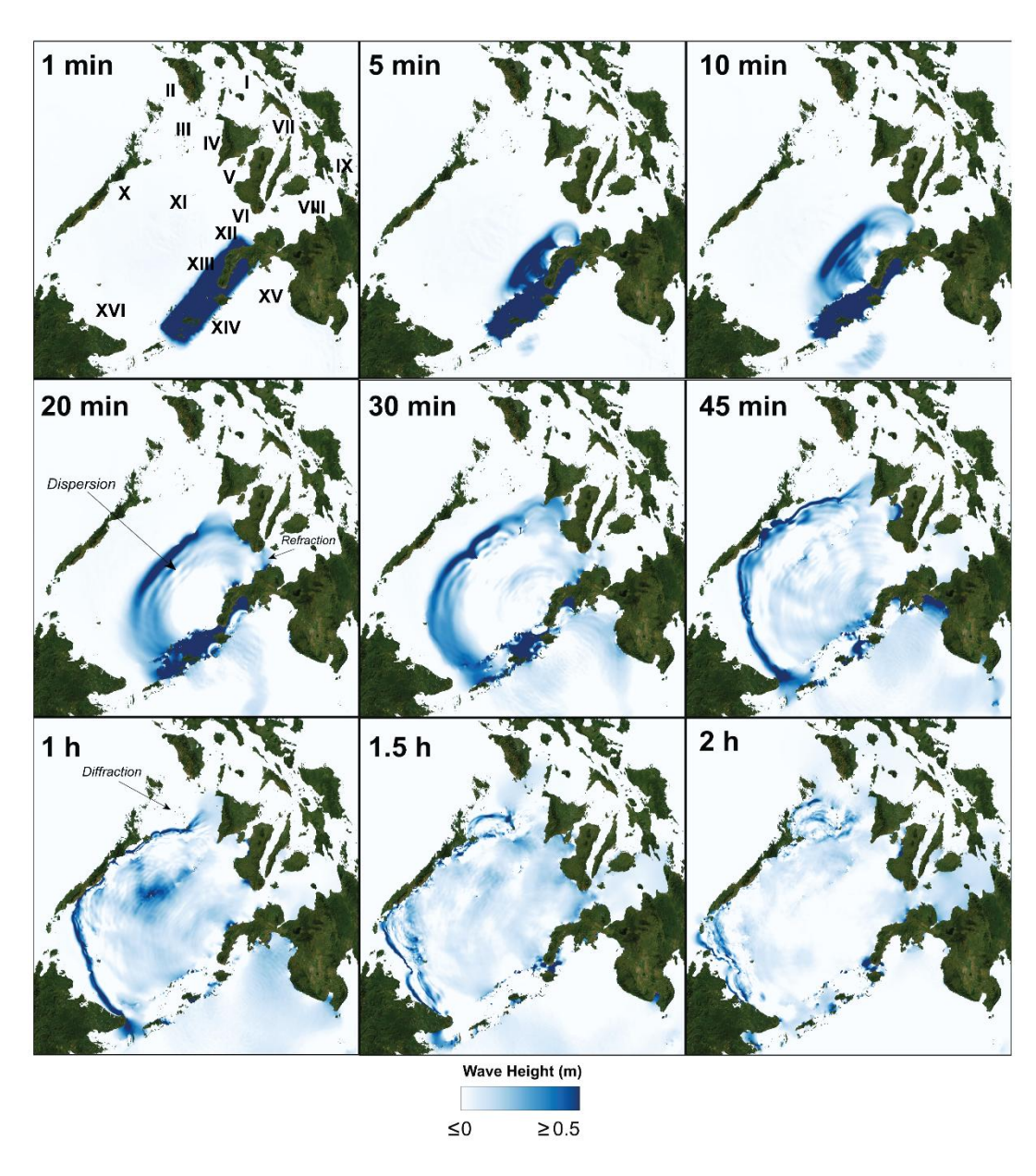


Figure 5. Tsunami wave (2 h) propagation from ST segment at 20° dip angle. Basemap from World Imagery.





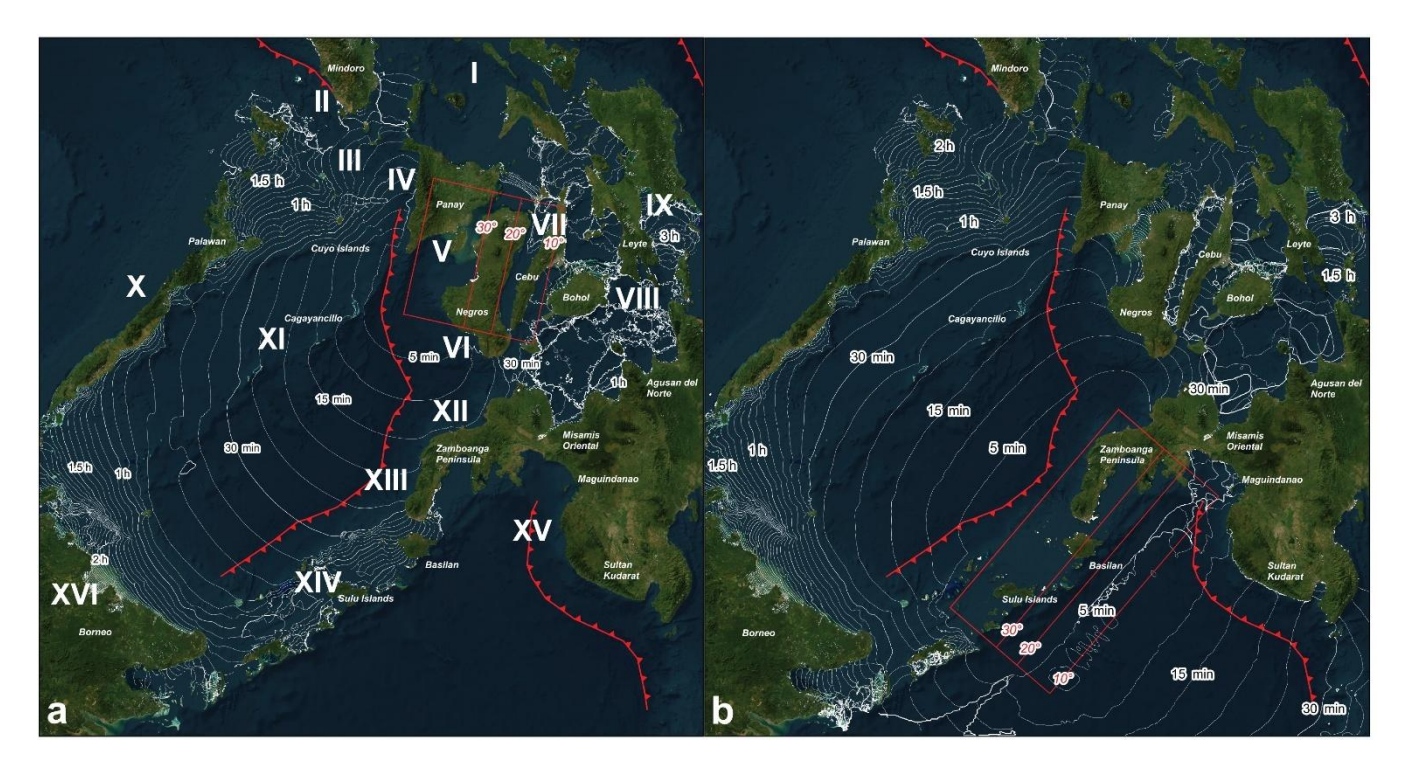


Figure 6. Tsunami wave arrival times from (a) NT1-1 and (b) ST segments. Contours have 5-min intervals. I-XI indicate the 16 coastal regions described in Fig. 4. Basemap from World Imagery.





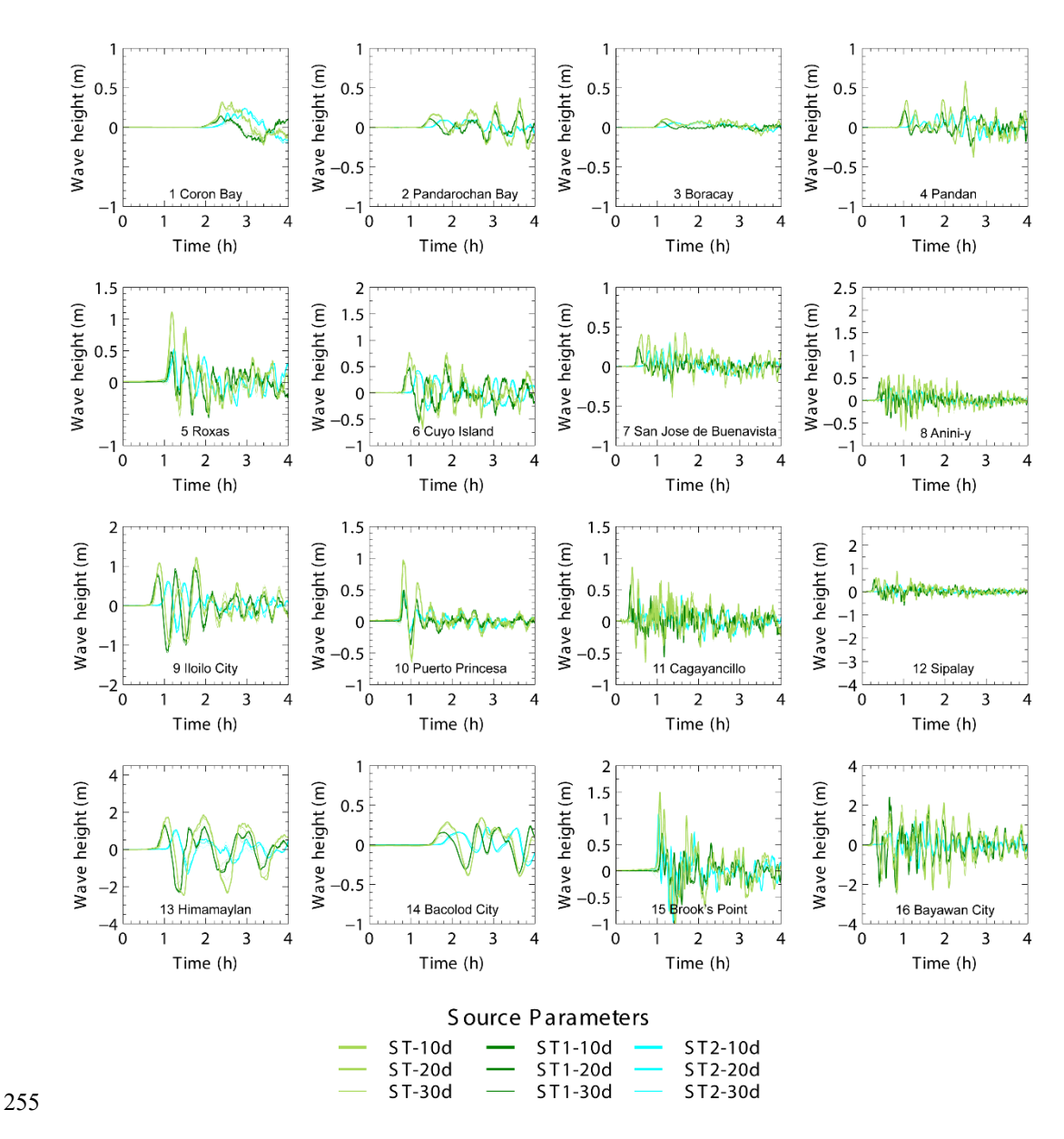


Figure 7. Tsunami waveforms in TGS 1-16 from Sulu Trench segments (see Fig. 4 for locations).





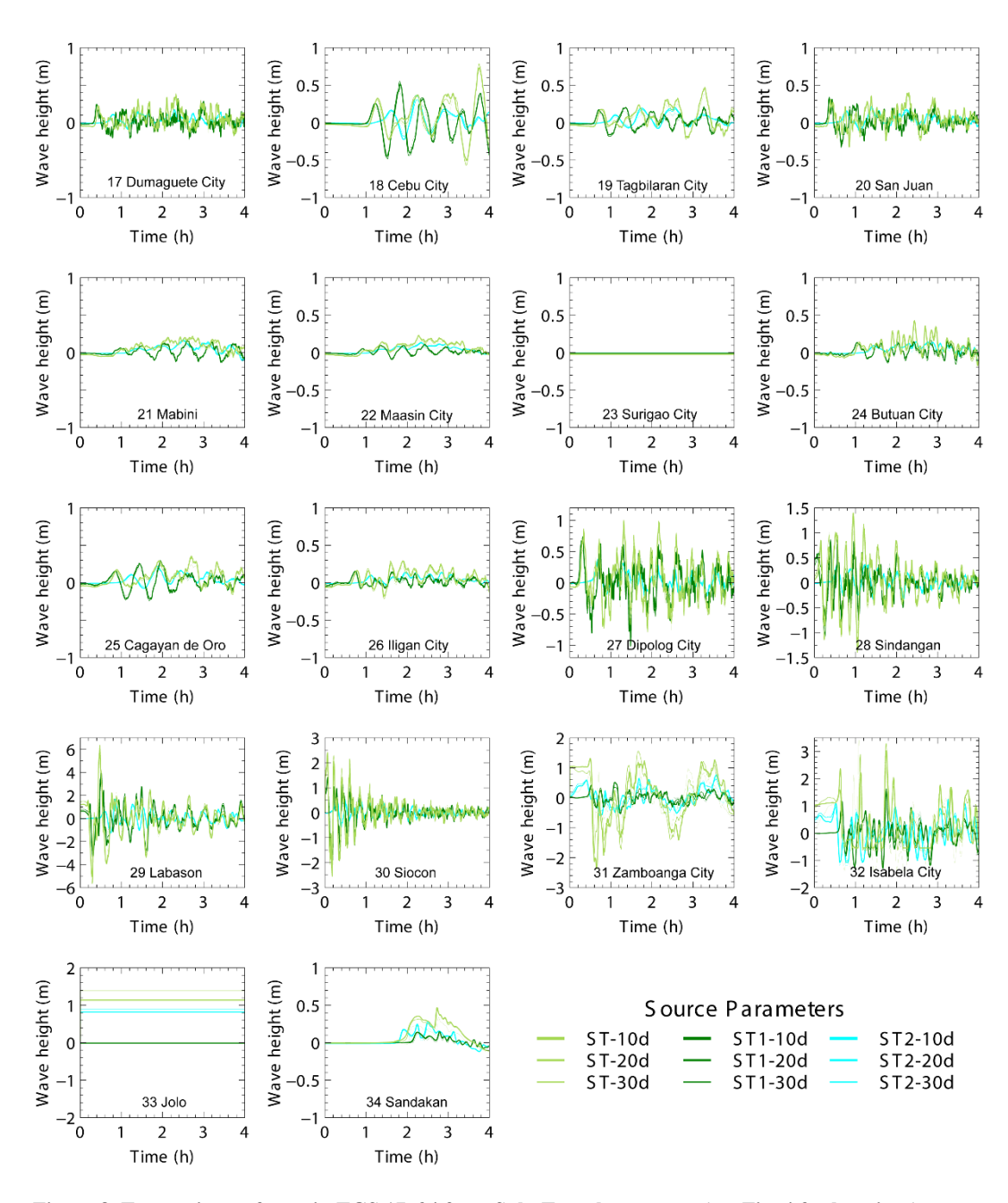


Figure 8. Tsunami waveforms in TGS 17-34 from Sulu Trench segments (see Fig. 4 for locations).





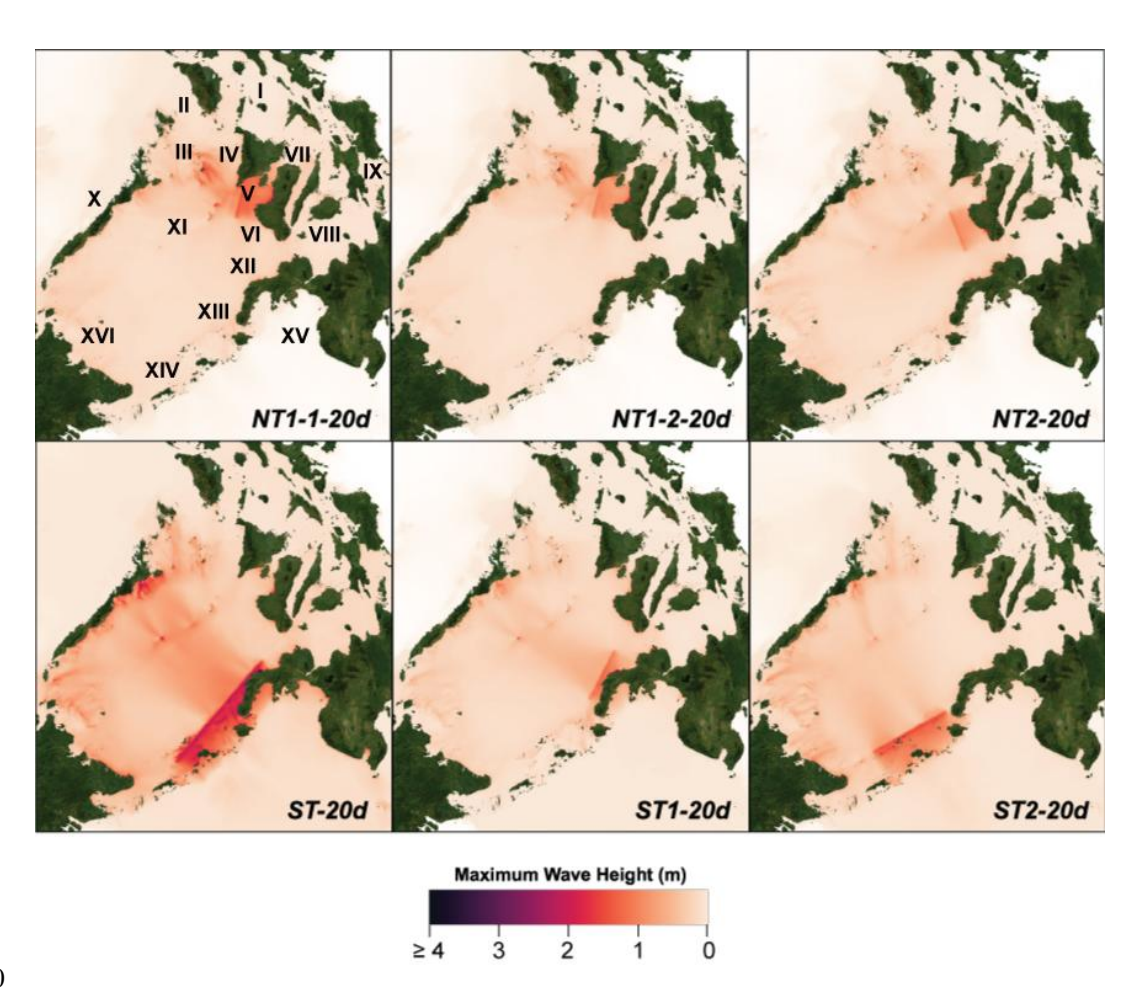


Figure 9. Maximum wave height (m) from the 4-h tsunami simulation of six segments with a megathrust dipping at 20°. Basemap from World Imagery.





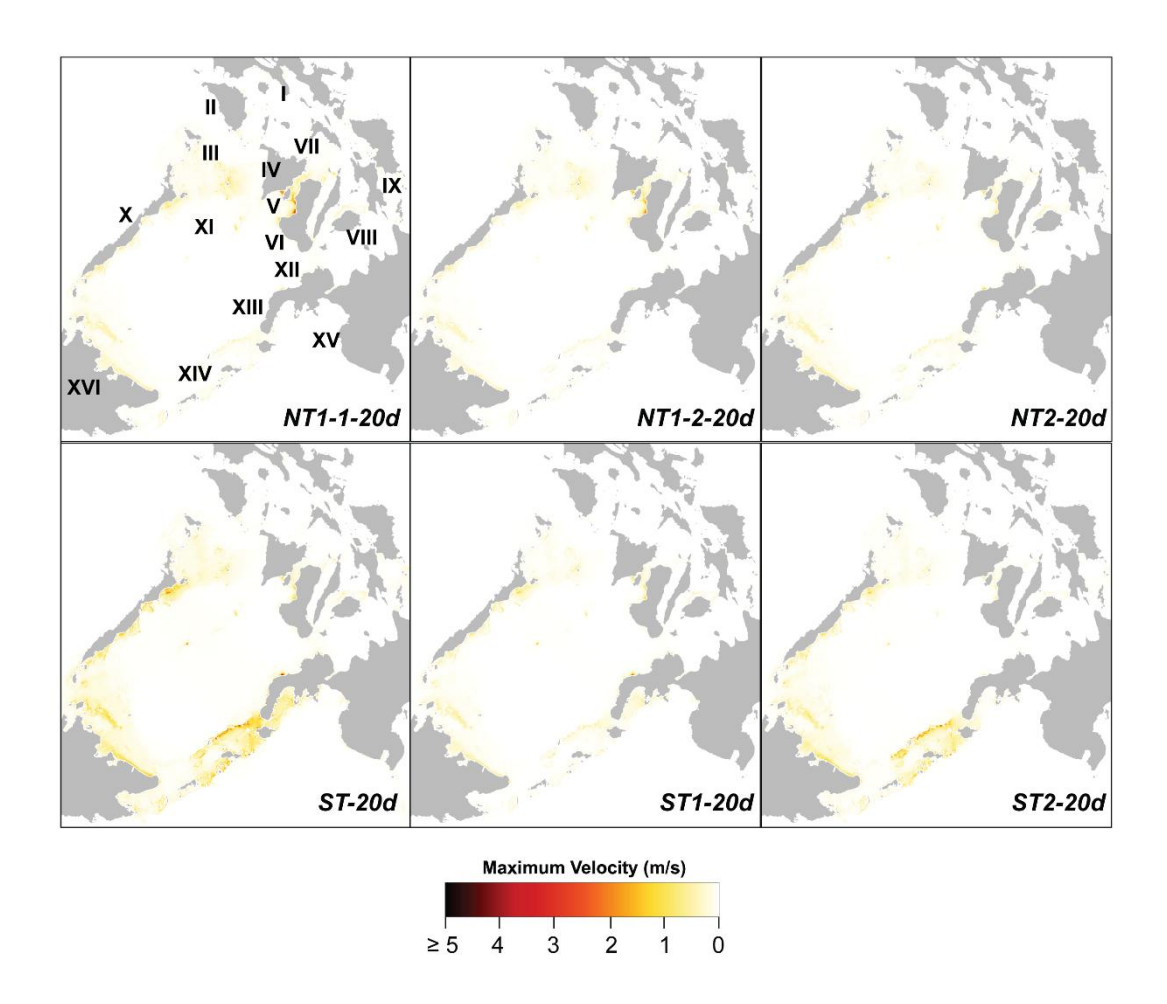


Figure 10. Maximum flow velocity (m/s) from the 4-h tsunami simulation of six segments with a megathrust dipping at 20°.

Table 2. Statistics of the maximum wave height and flow velocity difference comparing 10°-dip megathrust with 20° and 30°.

	Comparison relative to 10° slab	Maxim	um Wave Hei	ght Differe	nce	Maximum Flow Velocity Difference				
Segment		Max (m)	Mean (m)	Min (m)	σ (m)	Max (m/s)	Mean (m/s)	Min (m/s)	σ (m/s)	
NT1-1	10° v 20°	1.108	0.017	-0.970	0.044	1.811	0.071	-1.774	0.023	
N11-1	10° v 30°	1.286	0.038	-0.731	0.063	1.811	0.009	-2.140	0.033	
NT1 2	10° v 20°	0.934	0.104	-0.655	0.027	1.299	0.002	-1.099	0.012	
NT1-2	10° v 30°	1.979	0.025	-0.529	0.039	1.369	0.005	-1.576	0.019	





		1							
NT2	10° v 20°	2.501	0.008	-0.862	0.012	0.968	0.002	-1.652	0.010
1112	10° v 30°	2.507	0.020	-1.141	0.035	1.134	0.004	-1.439	0.016
ST	10° v 20°	4.684	0.063	-1.144	0.131	4.154	0.009	-1.357	0.053
	10° v 30°	5.622	0.116	-1.890	0.172	4.509	0.017	-2.164	0.077
ST1	10° v 20°	2.944	0.014	-0.826	0.038	2.583	0.003	-1.020	0.023
	10° v 30°	3.395	0.036	-0.857	0.058	2.675	0.006	-1.088	0.034
ST2	10° v 20°	2.289	0.038	-0.481	0.085	2.369	0.004	-1.067	0.025
	10° v 30°	3.206	0.071	-1.164	0.106	3.135	0.010	-1.069	0.037





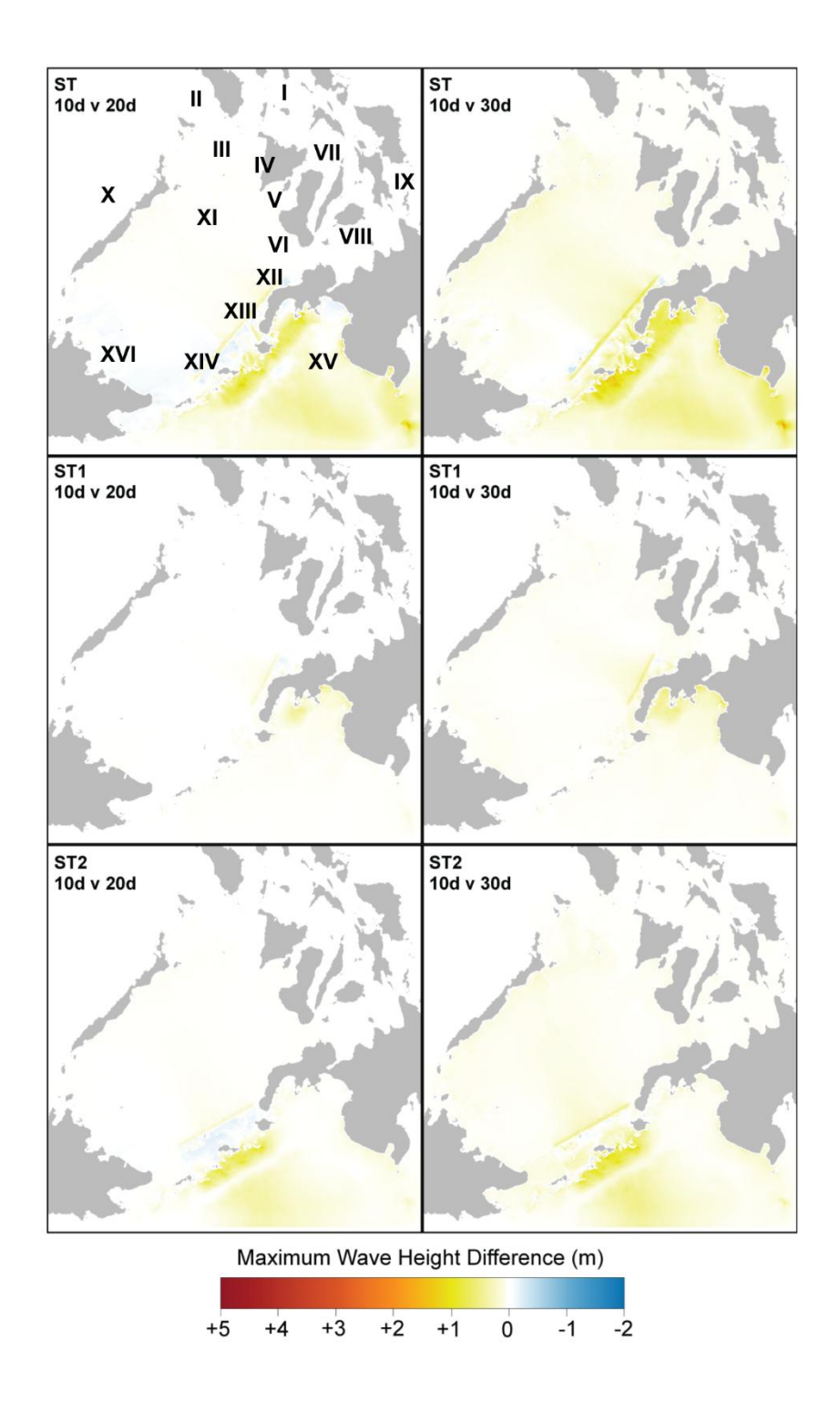


Figure 11. Maximum wave height difference from 10°-dip megathrust compared to that of 20° and 30° in the Sulu Trench segments.





#### 5 Discussion

275

280

285

#### 5.1 Influence of Wave Directivity, Coastal Morphology, and Nearshore Width on Maximum Wave Height

Wave directivity mainly controls the distribution of the highest tsunami wave heights, which are coastal regions directly facing (i.e., V, VI, XII, XIII, XIV, XV) and on the rear side (III, X) of the segments. As tsunami waves propagate in the interior central Philippines, wave interactions, refraction, diffraction, reflection, and nonlinear effects result in significant dissipation, with the majority of coastal areas in I, VII, XIII, and IX having <1 m wave height. However, the morphology of coastlines, especially along embayments, can amplify tsunamis due to constructive resonance, which can even generate up to 2 m in interior islands (Figure 12b–f). Previous studies have also acknowledged the effects of morphology on tsunami wave resonance (e.g., Aranguiz et al., 2019; Roeber et al., 2010; Vela et al., 2014; Yamazaki & Cheung, 2011).

The foremost islands can also function as a natural barrier for the rear islands as they diffract and attenuate the tsunami waves. This case is apparent for the higher tsunami waves in III compared to its rear islands (**Figure 12g**). Another factor playing a role in the resulting tsunami waves is the nearshore width along the coasts, as nonlinear shallow-water waves dominate. Arbitrarily setting the distance between the -50 m and 0 m depth contour as a reference for nearshore width in 6,879 sampling points, the nearshore width interquartile range of the coastal areas with ≥2 m maximum wave height is 2–4.5 km at a maximum bound of 8 km (**Figure 13**). On the other hand, coastal areas with <2 m maximum wave height have a nearshore width interquartile range of 2.8–10.6 km with a maximum bound of 22 km. All coastal areas with nearshore width ranging from 30 to 77 km also have <2 m maximum wave height. This indicates that as the nearshore width widens (e.g., >20 km), wave dissipation increases, reducing the tsunami wave as it reaches the shoreline. This is exemplified in the difference in distribution of maximum tsunami wave heights between the northern and southern coastline of XVI (**Figure 12h**).





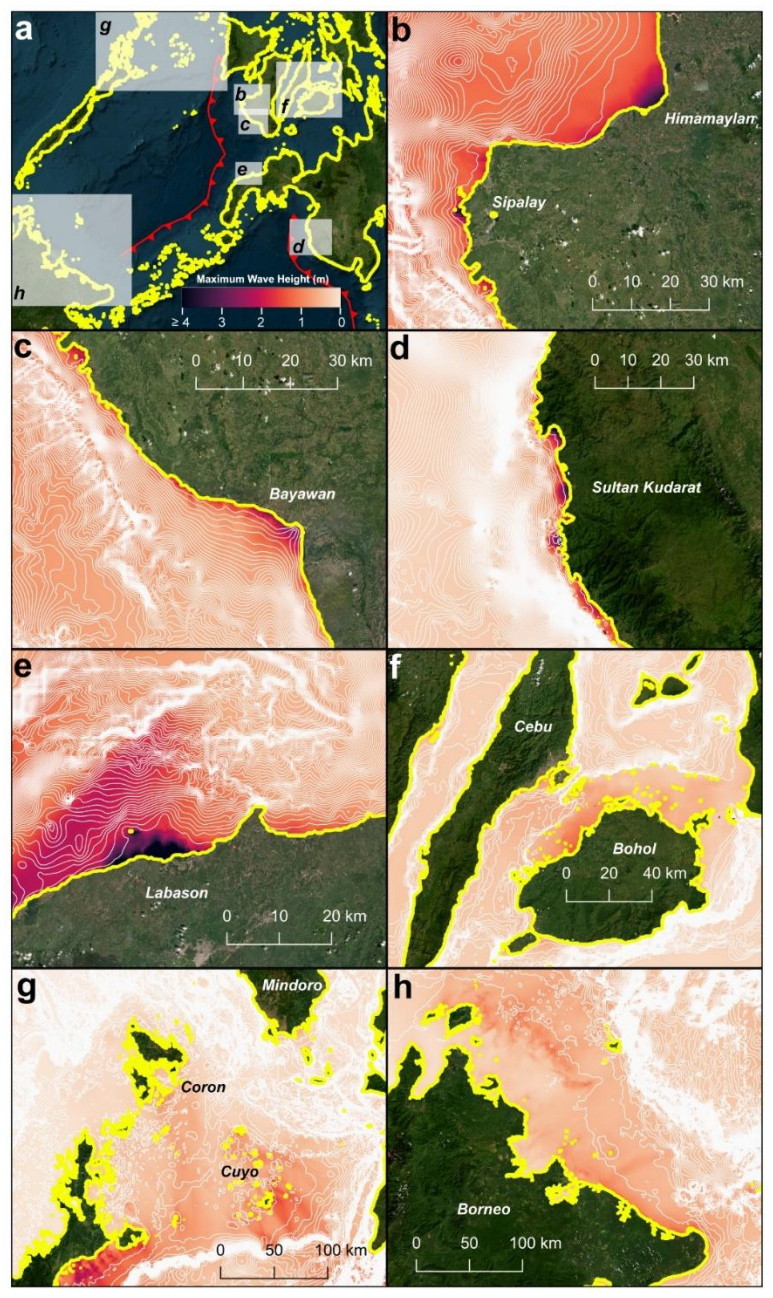


Figure 12. Representative sites highlighting the influence of nearshore bathymetry on the maximum wave height among 18 segment scenarios. (a) Inset maps of Figure 4.24b–h. The white contours of the bathymetry from GEBCO have 50 m intervals. (b–d) southwest Negros (VI), (e) Labason (XII), (f) northern Bohol (VII), (g) Coron Islands (III), and (h) northeast Borneo (XVI). Basemap from World Imagery.





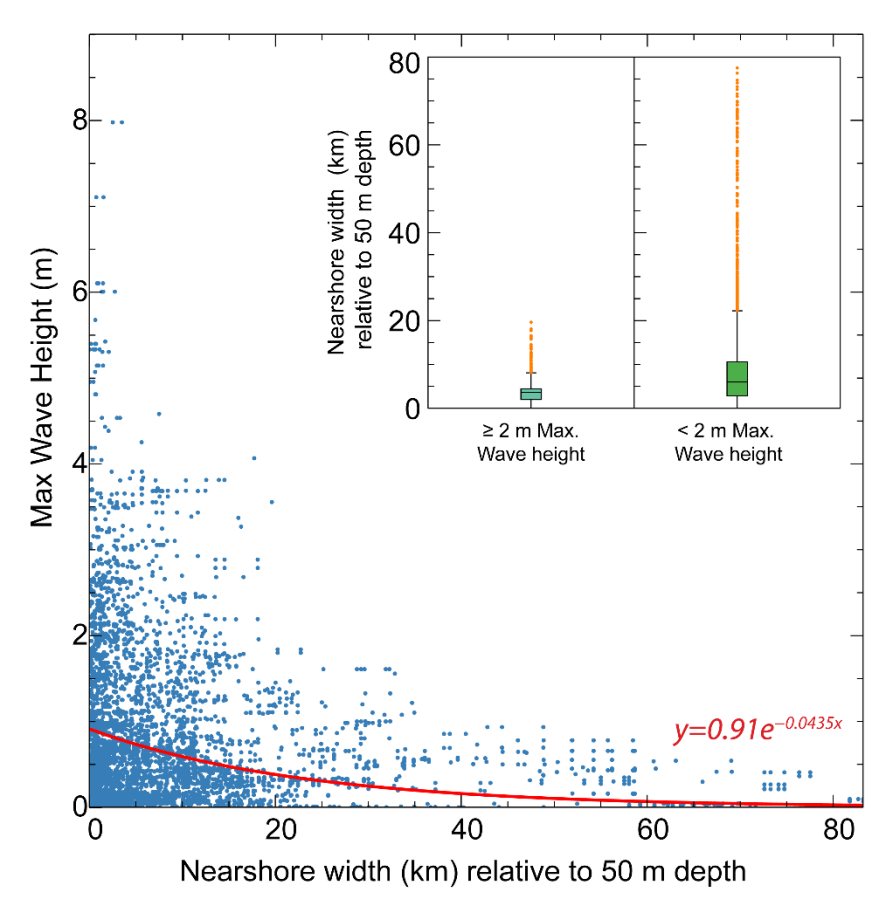


Figure 13. Maximum tsunami wave height from 6,879 sampling points across the coastal regions in central and southern Philippines and the corresponding nearshore width (km) relative to 50 m depth. Boxplots show the interquartile range (1.5IQR) of nearshore width between coastlines with  $\geq$ 2 m and <2 m maximum tsunami wave height. Orange circles indicate the outliers of the interquartile range.

## 5.2 Implications for Tsunami Hazard Potential

Accounting for all 18 megathrust rupture scenarios, **Figure 14**, **S15**, and **S16** present the maximum wave height (m), flow velocity (m/s), and minimum arrival times (min), respectively, in coastal areas surrounding the Sulu Sea. Of the 6,879 sampling points, 8% have a maximum wave height of ≥2 m. Sindangan–Labason (XII) and Siocon–Sibuco (XIII), Sipalay – Bayawan (VI), Moro Gulf (XV), and Basilan–Sulu (XIV) have the highest exposure of 5–8 m wave height and 5–7 m/s flow velocity. Certain coastlines in Palawan (X), Panay Gulf (V), Coron–Cuyo (III), West Panay (IV), northeast Borneo (XVI), and Bohol Sea (III) are potentially exposed to 2–4 m wave height and 2–4 m/s flow velocity. The majority of Tañon–Cebu Strait (VII), Mindoro (II), Leyte Gulf (IX), and Visayan Sea (I) coastal regions have a maximum wave height and flow velocity of <1 m and <1 m/s, respectively, with minor amplification of up to 2 m and 2 m/s in a few areas. Comparisons of wave heights across 16 coastal regions are also shown in **Figure 15** with an average ranging from 0.1 m to 2.1 m and standard deviations of ±0.06–0.77 m.

The majority of coastal regions with the highest tsunami waves (XII, XIII, VI, XV, XIV) also have the shortest arrival times of <2 min due to their proximity to the rupture segments. This short arrival requires the need for quick evacuation strategies. In certain areas where established evacuation sites are far, vertical evacuation, i.e., reaching the closest elevated and

295

300

305



320

330

335

340



structurally strong location, may be the most viable option. While the variability of coastal surface roughness is not accounted for in these models, pre-existing natural and man-made barriers may delay or inhibit inundation, providing additional time for evacuation.

A major limitation of this study is the uniform slip distribution along the megathrust fault plane, which is based on the average slip from the scaling equation. Earthquake slip distributions are typically heterogeneous, and they control whether the initial seafloor displacement can generate tsunamis. Megathrust ruptures with larger slip distributions downdip but lower on the updip can produce lower tsunami waves (e.g., Delouis et al., 2010; Fujii et al., 2020), which can lead to overestimation from these rupture scenarios. Conversely, large slip updip, especially for trench-breaching and splay faulting rupture types, can produce larger seafloor displacement (e.g., Baba et al., 2006; Fujiwara et al., 2011) that may underestimate the resulting tsunami wave heights from this study. Splay faulting and trench-breaching megathrust scenarios are also not accounted for in this study, as these modes of rupture are rarely reported, but they must be considered in future tsunami hazard assessments in this subduction zone. While the geometry of the Negros–Sulu subduction zone is currently not well constrained, the generally thick sediment cover overlying the Negros and Sulu subduction zone (Figure 1) may decrease the slab dip and can widen the seismogenic zone (Brizzi et al., 2020).

The use of single-fault models with uniform slip distributions in this study can serve as baseline information in light of the scarcity of geodetic data for finite-fault slip models. The calculated maximum slip can also serve as a reference in future work that will apply heterogeneous and stochastic slip distributions. Notably, misfit analyses on the use of uniform slip models from past tsunami events (An et al., 2018; Nakata et al., 2019) have found acceptable prediction errors, suggesting the effectiveness of this approach in identifying highly exposed coastal areas.

Future studies along the Negros–Sulu subduction zone should aim to constrain both the geometry of the subduction slab and coupling ratios where slip deficits can be derived as applied in other subduction zones (e.g., Chlieh et al., 2008; Métois et al., 2013, 2016; Michel et al., 2019; Moreno et al., 2010; Ozawa et al., 2012). The role of submarine landslides in tsunami generation can also be explored in future studies as these features are prevalent in this active margin (Nawanao & Ramos, 2023). Submarine landslides have been shown to amplify tsunamis when the failure is coeval to megathrust earthquakes or can also be the main driver of localized but large tsunamis (e.g., Heinrich et al., 2001; Imamura et al., 1995; Nakata et al., 2020; Ramirez et al., 2022; Schambach et al., 2020; Takagi et al., 2019). Tsunamis driven by outer rise faulting may also be possible as focal mechanism solutions indicate normal faulting along these sections of the subduction zone (**Figure 2**).

Updated seismic reflection and geophysical surveys across the Negros–Sulu Trench may also reveal underlying complexities that can influence the potential to generate megathrust rupture, including splay faults, fluids, and subducting seamounts. The accuracy of nearshore bathymetry connecting inland and offshore must also be assessed, as the nearshore width shown in this study has significant effects on the resulting maximum tsunami waves along the coasts. Furthermore, mapping of pre-existing natural and man-made barriers for site-specific simulation and vulnerability assessment will also be important to assess their effectiveness in minimizing tsunami inundation.

The identified localities with the highest exposure to tsunami waves are potential sites (e.g., V, VI, XII, XIII) in searching for paleotsunami deposits that may serve as records for prehistoric earthquakes. Most importantly, the estimated moment magnitude, maximum tsunami wave heights, flow velocity, and minimum arrival times can provide invaluable information in creating strategies and policies for local government offices and coastal communities to mitigate hazard risk. These include information dissemination in coastal communities, delineation of evacuation routes and sites, and proper engineering designs such as coastal forests, green embankments, seawalls, offshore breakwaters, and dikes (e.g., Benazir et al., 2024; Dengler, 2005; Oetjen et al., 2022; Strusińska-Correia, 2017).

355





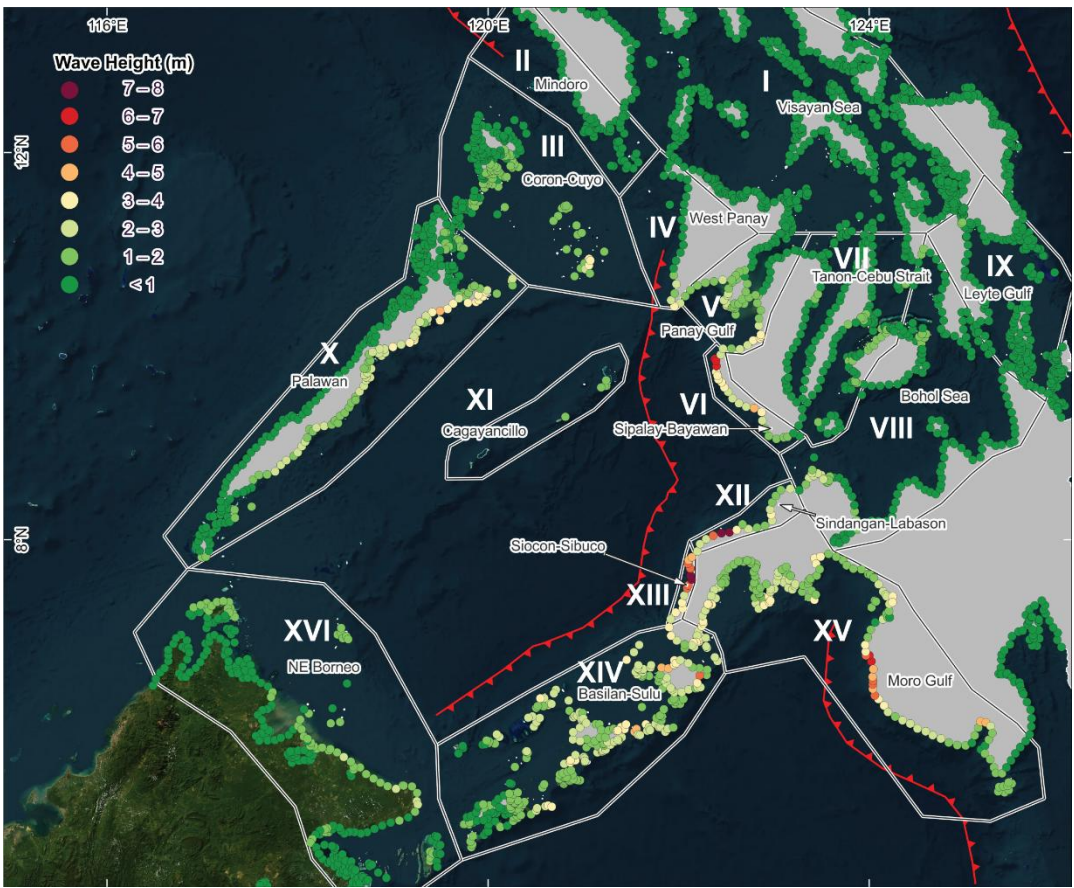


Figure 14. Exposure map of coastal regions in central and southern Philippines of the highest maximum wave height from the 18 megathrust rupture scenarios. The 6,879 sampling points have a 10 km interval. Basemap from World Imagery.





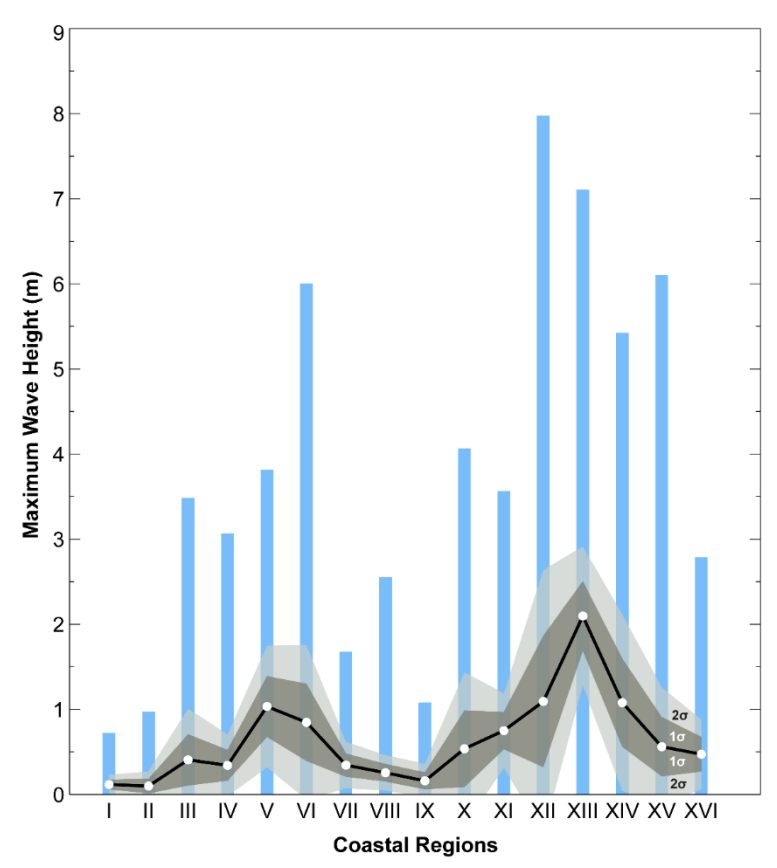


Figure 15. Comparisons of maximum wave heights among the 16 coastal regions. White circles and blue bars indicate the mean and maximum values, respectively, while the envelope indicates the 1σ and 2σ standard deviations. I, Visayan Sea; II, Mindoro; III, Coron–Cuyo; IV, West Panay; V, Panay Gulf; VI, Sipalay–Bayawan; VII, Tanon–Cebu Strait; VIII, Bohol Sea; IX, Leyte Gulf; X, Palawan; XI, Cagayancillo; XII, Sindangan–Labason; XIII, Siocon–Sibuco; XIV, Basilan–Sulu; XV, Moro Gulf; XVI, northeast Borneo.

## 6 Conclusion

365

370

375

380

We modeled the fault rupture and tsunami hazard potential of the Negros–Sulu subduction zone by constraining six megathrust fault segments at three dip angle scenarios (10°, 20°, and 30°). Rupture-scaling equations using the fault plane area estimate potential magnitude ranging from Mw 8.0 to 8.6 for the Negros Trench and Mw 8.1 to 8.9 for the Sulu Trench segments. From the estimated source parameters, elastic dislocation, and 4-h tsunami simulation, coastal areas directly facing the trench segments (VI Sipalay–Bayawan, XII Sindangan–Labason, XIII Siocon–Sibuco, XIV Basilan–Sulu, XV Moro Gulf) segments are potentially exposed to 5–8 m wave height and 5–7 m/s flow velocity with a minimum arrival time of <2 min in majority of these regions, demonstrating the major control of wave directivity. Coastal areas parallel and on the rear side of the trench (X Palawan, XI Cagayancillo) are prone to tsunami wave height and flow velocity of up to 2–4 m and 2–4 m/s, respectively. Due to the cumulative effects of wave dissipation, interference, diffraction, and refraction, interior and rearmost islands are also exposed to <2 m tsunami wave height and <2 m/s flow velocity. We also identified regions in the Sulu Sea where resonance on embayments can amplify tsunami waves, while nearshore width >30 km can lead to attenuation before reaching coastlines.

The multitude of future work reflects the scarcity of information along this active margin and the opportunity to fill these gaps. What this study provides, amid the limited information, are the exposure maps of the minimum arrival, maximum



385

395



tsunami wave, and flow velocity across the entire central and southern Philippines from different scenarios, informed based on available data and current understanding of megathrust ruptures. This new information is crucial not only for future studies to extend our records by searching paleotsunami deposits but most especially in mitigating the imminent threat of tsunamis that have severely affected the Philippines in the past.

#### **Code Availability**

The JAGURS code is available at <a href="https://github.com/jagurs-admin/jagurs">https://github.com/jagurs-admin/jagurs</a>.

#### **Data Availability**

390 Data can be accessed freely available under the Creative Commons Attribution 4.0 International license at Zenodo: <a href="https://10.5281/zenodo.17234831">https://10.5281/zenodo.17234831</a>.

#### **Author Contribution**

LN and NR conceptualized the study. LN conducted the tsunami modeling, formal analysis, and visualization. NR acquired the funding and administered the project. TB, NC, and KS were involved in the development of the JAGURS code. LN wrote the original draft. NR, TB, NC, and KS reviewed and edited the manuscript.

## **Competing Interests**

The authors declare that they have no conflict of interest.

#### Acknowledgments

Funding was provided by the Department of Science and Technology (DOST) through the project (No. 4233) titled "Investigation and Numerical Modeling of Philippine Tsunamis Based on Historical, Geomorphological, and Geological Evidence of Past Earthquakes Investigation and Numerical Modeling of Philippine Tsunamis" of NR. We thank the project team, including Alec Benjamin G. Ramirez, Jelian S. Reyes, and Robelyn Z. Mangahas—Flores, as well as the members of the UP NIGS Geomorphology and Active Tectonics Research (GEAR) Laboratory for their contribution to this project. The maps in the paper were generated in QGIS. The World Imagery basemap is from Esri, DigitalGlobe, GeoEye, i-cubed, USDA FSA, USGS, AEX, Getmapping, Aerogrid, IGN, IGP, swisstopo, and the GIS User Community. This study forms part of LN's Master's thesis, "From Trench to Coast: Investigating the Late Quaternary Tectonic History and Seismic Hazard Potential of the Negros—Sulu Trench System, Philippines", conducted at the University of the Philippines Diliman.

### References

Acharya, H. K. (1978). Mindanao earthquake of August 16, 1976: Preliminary seismological assessment. *Bulletin of the Seismological Society of America*, 68(5), 1459–1468. https://doi.org/10.1785/BSSA0680051459

Allen, T. I., & Hayes, G. P. (2017). Alternative rupture-scaling relationships for subduction interface and other offshore environments. *Bulletin of the Seismological Society of America*, 107(3), 1240–1253. https://doi.org/10.1785/0120160255
 An, C., Liu, H., Ren, Z., & Yuan, Y. (2018). Prediction of Tsunami Waves by Uniform Slip Models. *Journal of Geophysical Research: Oceans*, 123(11), 8366–8382. https://doi.org/10.1029/2018JC014363





- Aranguiz, R., Catalán, P. A., Cecioni, C., Bellotti, G., Henriquez, P., & González, J. (2019). Tsunami Resonance and Spatial Pattern of Natural Oscillation Modes With Multiple Resonators. *Journal of Geophysical Research: Oceans*, 124(11), 7797–7816. https://doi.org/10.1029/2019JC015206
  - Athukorala, P., & Resosudarmo, B. P. (2005). The Indian Ocean Tsunami: Economic Impact, Disaster Management, and Lessons. *Asian Economic Papers*, 4(1), 1–39. https://doi.org/10.1162/asep.2005.4.1.1
- 420 Aurelio, M. A. (2008). Shear partitioning in the Philippines: Constraints from Philippine Fault and global positioning system data. *Island Arc*, 9(4), 584–597. https://doi.org/10.1111/j.1440-1738.2000.00304.x
  - Aurelio, M. A., Peña, R. E., & Taguibao, K. J. L. (2013). Sculpting the Philippine archipelago since the Cretaceous through rifting, oceanic spreading, subduction, obduction, collision and strike-slip faulting: Contribution to IGMA5000. *Journal of Asian Earth Sciences*, 72, 102–107. https://doi.org/10.1016/j.jseaes.2012.10.007
- Baba, T., Allgeyer, S., Hossen, J., Cummins, P. R., Tsushima, H., Imai, K., Yamashita, K., & Kato, T. (2017). Accurate numerical simulation of the far-field tsunami caused by the 2011 Tohoku earthquake, including the effects of Boussinesq dispersion, seawater density stratification, elastic loading, and gravitational potential change. *Ocean Modelling*, 111, 46–54. https://doi.org/10.1016/j.ocemod.2017.01.002
- Baba, T., Cummins, P. R., Hori, T., & Kaneda, Y. (2006). High precision slip distribution of the 1944 Tonankai earthquake inferred from tsunami waveforms: Possible slip on a splay fault. *Tectonophysics*, 426(1–2), 119–134. https://doi.org/10.1016/j.tecto.2006.02.015
  - Baba, T., Takahashi, N., Kaneda, Y., Ando, K., Matsuoka, D., & Kato, T. (2015). Parallel Implementation of Dispersive Tsunami Wave Modeling with a Nesting Algorithm for the 2011 Tohoku Tsunami. *Pure and Applied Geophysics*, 172(12), 3455–3472. https://doi.org/10.1007/s00024-015-1049-2
- 435 Badillo, V. L., & Astilla, Z. C. (1978). *Moro Gulf Tsunami of 17 August 1976*. National Committee on Marine Sciences (Philippines). Special Committee on Tsunami Warning System.
  - Balmino, G., Vales, N., Bonvalot, S., & Briais, A. (2012). Spherical harmonic modelling to ultra-high degree of Bouguer and isostatic anomalies. *Journal of Geodesy*, 86(7), 499–520. https://doi.org/10.1007/s00190-011-0533-4
  - Bautista, M. L. P., Bautista, B. C., Joan, S., & Narag, I. (2012). Philippine Tsunamis and Seiches (1589-2012).
- Benazir, Triatmadja, R., Syamsidik, Nizam, & Warniyati. (2024). Vegetation-based approached for tsunami risk reduction: Insights and challenges. *Progress in Disaster Science*, 23, 100352. https://doi.org/10.1016/j.pdisas.2024.100352
  - Bletery, Q., Thomas, A. M., Rempel, A. W., Karlstrom, L., Sladen, A., & De Barros, L. (2016). Mega-earthquakes rupture flat megathrusts. *Science*, 354(6315), 1027–1031. https://doi.org/10.1126/science.aag0482
- Bondár, I., Engdahl, E. R., Villaseñor, A., Harris, J., & Storchak, D. (2015). ISC-GEM: Global Instrumental Earthquake
  Catalogue (1900–2009), II. Location and seismicity patterns. *Physics of the Earth and Planetary Interiors*, 239, 2–13. https://doi.org/10.1016/j.pepi.2014.06.002
  - Brizzi, S., van Zelst, I., Funiciello, F., Corbi, F., & van Dinther, Y. (2020). How Sediment Thickness Influences Subduction Dynamics and Seismicity. *Journal of Geophysical Research: Solid Earth*, 125(8), 1–19. https://doi.org/10.1029/2019JB018964
- 450 Brocher, T. M., Filson, J. R., Fuis, G. S., Haeussler, P. J., Holzer, T. L., Plafker, G., & Blair, J. L. (2014). *The 1964 Great Alaska Earthquake and tsunamis: a modern perspective and enduring legacies* (Fact Sheet). https://doi.org/10.3133/fs20143018
  - Chlieh, M., Avouac, J. P., Sieh, K., Natawidjaja, D. H., & Galetzka, J. (2008). Heterogeneous coupling of the Sumatran megathrust constrained by geodetic and paleogeodetic measurements. *Journal of Geophysical Research: Solid Earth*, 113(5), 1–31. https://doi.org/10.1029/2007JB004981
  - Claro, S. M. D., Ramos, N. T., Fernando, A. G. S., Ishimura, D., & Switzer, A. D. (2021). Sedimentological evidence of washover deposits from extreme wave events in Zamboanga del Sur, Mindanao, southern Philippines. *Marine Geology*, 438(April), 106535. https://doi.org/10.1016/j.margeo.2021.106535
- Delouis, B., Nocquet, J., & Vallée, M. (2010). Slip distribution of the February 27, 2010 Mw = 8.8 Maule Earthquake, central Chile, from static and high-rate GPS, InSAR, and broadband teleseismic data. *Geophysical Research Letters*, *37*(17), 1–7. https://doi.org/10.1029/2010GL043899
  - Dengler, L. (2005). The Role of Education in the National Tsunami Hazard Mitigation Program. *Natural Hazards*, 35(1), 141–153. https://doi.org/10.1007/s11069-004-2409-x
  - Di Giacomo, D., Bondár, I., Storchak, D. A., Engdahl, E. R., Bormann, P., & Harris, J. (2015). ISC-GEM: Global Instrumental





- Earthquake Catalogue (1900–2009), III. Re-computed M and m, proxy M, final magnitude composition and completeness assessment. *Physics of the Earth and Planetary Interiors*, 239, 33–47. https://doi.org/10.1016/j.pepi.2014.06.005
  - Di Giacomo, D., Engdahl, E. R., & Storchak, D. A. (2018). The ISC-GEM Earthquake Catalogue (1904–2014): status after the Extension Project. *Earth System Science Data*, 10(4), 1877–1899. https://doi.org/10.5194/essd-10-1877-2018
- 470 Duke, C. M. (1960). The Chilean Earthquakes of May 1960. *Science*, *132*(3442), 1797–1802. https://doi.org/10.1126/science.132.3442.1797
  - Fan, J., & Zhao, D. (2019). P-wave anisotropic tomography of the central and southern Philippines. *Physics of the Earth and Planetary Interiors*, 286(September 2018), 154–164. https://doi.org/10.1016/j.pepi.2018.12.001
- Fan, J., Zhao, D., Dong, D., & Zhang, G. (2017). P-wave tomography of subduction zones around the central Philippines and its geodynamic implications. *Journal of Asian Earth Sciences*, 146(February), 76–89. https://doi.org/10.1016/j.jseaes.2017.05.015
  - Fujii, Y., Satake, K., Watada, S., & Ho, T.-C. (2020). Slip distribution of the 2005 Nias earthquake (Mw 8.6) inferred from geodetic and far-field tsunami data. *Geophysical Journal International*, 223(2), 1162–1171. https://doi.org/10.1093/gji/ggaa384
- Fujiwara, T., Kodaira, S., No, T., Kaiho, Y., Takahashi, N., & Kaneda, Y. (2011). The 2011 Tohoku-Oki earthquake: Displacement reaching the trench axis. *Science*, 334(6060), 1240. https://doi.org/10.1126/science.1211554
  - Galgana, G., Hamburger, M., McCaffrey, R., Corpuz, E., & Chen, Q. (2007). Analysis of crustal deformation in Luzon, Philippines using geodetic observations and earthquake focal mechanisms. *Tectonophysics*, 432(1–4), 63–87. https://doi.org/10.1016/j.tecto.2006.12.001
- 485 GEBCO Compilation Group. (2024). *GEBCO 2024 Grid.* https://doi.org/.5285/12345678-90ab-cdef-1234-567890abcdef Hayes, G. P., Moore, G. L., Portner, D. E., Hearne, M., Flamme, H., Furtney, M., & Smoczyk, G. M. (2018). Slab2, a comprehensive subduction zone geometry model. *Science*, *362*(6410), 58–61. https://doi.org/10.1126/science.aat4723
  - Heinrich, P. H., Piatanesi, A., & Hébert, H. (2001). Numerical modelling of tsunami generation and propagation from submarine slumps: The 1998 Papua New Guinea event. *Geophysical Journal International*, 145(1), 97–111. https://doi.org/10.1111/j.1365-246X.2001.00336.x
  - Hilde, T. W. C., Uyeda, S., & Kroenke, L. (1977). Evolution of the western pacific and its margin. *Tectonophysics*, 38(1–2). https://doi.org/10.1016/0040-1951(77)90205-0
  - Holloway, R., & Hall, R. (1996). Reconstructing Cenozoic SE Asia. *Geological Society Special Publication*, 106(106), 153–184. https://doi.org/10.1144/GSL.SP.1996.106.01.11
- 495 Hsu, Y.-J., Yu, S.-B., Loveless, J. P., Bacolcol, T., Solidum, R., Luis, A., Pelicano, A., & Woessner, J. (2016). Interseismic deformation and moment deficit along the Manila subduction zone and the Philippine Fault system. *Journal of Geophysical Research: Solid Earth*, 121(10), 7639–7665. https://doi.org/10.1002/2016JB013082
  - Hsu, Y.-J., Yu, S.-B., Song, T.-R. A., & Bacolcol, T. (2012). Plate coupling along the Manila subduction zone between Taiwan and northern Luzon. *Journal of Asian Earth Sciences*, *51*, 98–108. https://doi.org/10.1016/j.jseaes.2012.01.005
- 500 Imamura, F., Gica, E., Takahashi, T., & Shuto, N. (1995). Numerical simulation of the 1992 Flores tsunami: Interpretation of tsunami phenomena in northeastern Flores Island and damage at Babi Island. *Pure and Applied Geophysics PAGEOPH*, 144(3–4), 555–568. https://doi.org/10.1007/BF00874383
  - Kajitani, Y., Chang, S. E., & Tatano, H. (2013). Economic Impacts of the 2011 Tohoku-Oki Earthquake and Tsunami. *Earthquake Spectra*, 29(1 suppl), 457–478. https://doi.org/10.1193/1.4000108
- Kreemer, C., Blewitt, G., & Klein, E. C. (2014). A geodetic plate motion and Global Strain Rate Model. *Geochemistry, Geophysics, Geosystems*, 15(10), 3849–3889. https://doi.org/10.1002/2014GC005407
  - Laske, G., Masters, G., Ma, Z., & Pasyanos, M. (2013). Update on CRUST1.0 A 1-degree Global Model of Earth's Crust. EGU General Assembly Conference Abstracts. https://doi.org/2013EGUGA..15.2658L
- Li, L., Switzer, A. D., Chan, C., Wang, Y., Weiss, R., & Qiu, Q. (2016). How heterogeneous coseismic slip affects regional probabilistic tsunami hazard assessment: A case study in the South China Sea. *Journal of Geophysical Research: Solid Earth*, 121(8), 6250–6272. https://doi.org/10.1002/2016JB013111
  - Métois, M., Socquet, A., Vigny, C., Carrizo, D., Peyrat, S., Delorme, A., Maureira, E., Valderas-Bermejo, M.-C., & Ortega, I. (2013). Revisiting the North Chile seismic gap segmentation using GPS-derived interseismic coupling. *Geophysical Journal International*, 194(3), 1283–1294. https://doi.org/10.1093/gji/ggt183





- Métois, M., Vigny, C., & Socquet, A. (2016). Interseismic Coupling, Megathrust Earthquakes and Seismic Swarms Along the Chilean Subduction Zone (38°–18°S). *Pure and Applied Geophysics*, 173(5), 1431–1449. https://doi.org/10.1007/s00024-016-1280-5
  - Michel, S., Gualandi, A., & Avouac, J. P. (2019). Interseismic Coupling and Slow Slip Events on the Cascadia Megathrust. *Pure and Applied Geophysics*, 176(9), 3867–3891. https://doi.org/10.1007/s00024-018-1991-x
- 520 Moreno, M., Rosenau, M., & Oncken, O. (2010). 2010 Maule earthquake slip correlates with pre-seismic locking of Andean subduction zone. *Nature*, 467(7312), 198–202. https://doi.org/10.1038/nature09349
  - Nakata, K., Hayashi, Y., Tsushima, H., Fujita, K., Yoshida, Y., & Katsumata, A. (2019). Performance of uniform and heterogeneous slip distributions for the modeling of the November 2016 off Fukushima earthquake and tsunami, Japan. *Earth, Planets and Space*, 71(1), 30. https://doi.org/10.1186/s40623-019-1010-1
- Nakata, K., Katsumata, A., & Muhari, A. (2020). Submarine landslide source models consistent with multiple tsunami records of the 2018 Palu tsunami, Sulawesi, Indonesia. *Earth, Planets and Space*, 72(1), 44. https://doi.org/10.1186/s40623-020-01169-3
  - Nawanao, L. P., & Ramos, N. T. (2023). Frontal wedge variations and controls of submarine landslides in the Negros–Sulu Trench System, Philippines. *Frontiers in Earth Science*, 11(March), 1–17. https://doi.org/10.3389/feart.2023.1054825
- Nishikawa, T., & Ide, S. (2014). Earthquake size distribution in subduction zones linked to slab buoyancy. November, 1–5. https://doi.org/10.1038/NGEO2279
  - Nurashid, N. I. I., Shibazaki, B., Fujii, Y., & Yanagisawa, H. (2013). Tsunami inundation modeling along the east coast of Sabah, Malaysia for potential earthquakes in Sulu sea. *Bulletin of the International Institute of Seismology and Earthquake Engineering*, 47(Mmd), 127–132.
- Oetjen, J., Sundar, V., Venkatachalam, S., Reicherter, K., Engel, M., Schüttrumpf, H., & Sannasiraj, S. A. (2022). A comprehensive review on structural tsunami countermeasures. *Natural Hazards*, 113(3), 1419–1449. https://doi.org/10.1007/s11069-022-05367-y
  - Okada, Y. (1985). Surface deformation due to shear and tensile faults in a half-space. *Bulletin of the Seismological Society of America*, 75(4), 1135–1154. https://doi.org/10.1785/BSSA0750041135
- Okal, E. A., Synolakis, C. E., & Kalligeris, N. (2011). Tsunami Simulations for Regional Sources in the South China and Adjoining Seas. *Pure and Applied Geophysics*, 168(6–7), 1153–1173. https://doi.org/10.1007/s00024-010-0230-x
  - Ozawa, S., Nishimura, T., Munekane, H., Suito, H., Kobayashi, T., Tobita, M., & Imakiire, T. (2012). Preceding, coseismic, and postseismic slips of the 2011 Tohoku earthquake, Japan. *Journal of Geophysical Research: Solid Earth*, 117(7). https://doi.org/10.1029/2011JB009120
- Parcutela, N. E., Dimalanta, C. B., Armada, L. T., & Yumul, G. P. (2020). PHILCRUST3.0: New constraints in crustal growth rate computations for the Philippine arc. *Journal of Asian Earth Sciences: X, 4*(May), 100032. https://doi.org/10.1016/j.jaesx.2020.100032
  - Pedersen, C., Latif, Z. A., & Lai, C. (2011). TSUNAMI MODELLING AND RISK MAPPING FOR EAST COAST OF SABAH, MALAYSIA. *Coastal Engineering Proceedings*, 1(32), 55. https://doi.org/10.9753/icce.v32.currents.55
- Peñarubia, H. C., Johnson, K. L., Styron, R. H., Bacolcol, T. C., Sevilla, W. I. G., Perez, J. S., Bonita, J. D., Narag, I. C., Solidum, R. U., Pagani, M. M., & Allen, T. I. (2020). Probabilistic seismic hazard analysis model for the Philippines. *Earthquake Spectra*, *36*(1 suppl), 44–68. https://doi.org/10.1177/8755293019900521
  - Qiu, Q., Li, L., Hsu, Y.-J., Wang, Y., Chan, C.-H., & Switzer, A. D. (2019). Revised earthquake sources along Manila trench for tsunami hazard assessment in the South China Sea. *Natural Hazards and Earth System Sciences*, *19*(7), 1565–1583. https://doi.org/10.5194/nhess-19-1565-2019
  - Ramirez, A. B. G., Ramos, N. T., Nawanao, L. P. J., Mangahas-Flores, R. Z., Narag, I. C., Baba, T., Chikasada, N., & Satake, K. (2022). An Earthquake-Triggered Submarine Mass Failure Mechanism for the 1994 Mindoro Tsunami in the Philippines: Constraints from Numerical Modeling and Submarine Geomorphology. *Frontiers in Earth Science*, 10(November), 1–20. https://doi.org/10.3389/feart.2022.1067002
- Ramos, N. T., Maxwell, K. V., Tsutsumi, H., Chou, Y.-C., Duan, F., Shen, C.-C., & Satake, K. (2017). Occurrence of 1 kaold corals on an uplifted reef terrace in west Luzon, Philippines: Implications for a prehistoric extreme wave event in the South China Sea region. *Geoscience Letters*, 4(1), 12. https://doi.org/10.1186/s40562-017-0078-3
  - Rangin, C., Le Pichon, X., Mazzotti, S., Pubellier, M., Chamot-Rooke, N., Aurelio, M., Walpersdorf, A., & Quebral, R. (1999).

    Plate convergence measured by GPS across the Sundaland/Philippine Sea Plate deformed boundary: the Philippines and



570

575

590

595

600



- 565 eastern Indonesia. *Geophysical Journal International*, 139(2), 296–316. https://doi.org/10.1046/j.1365-246x.1999.00969.x
  - Roeber, V., Yamazaki, Y., & Cheung, K. F. (2010). Resonance and impact of the 2009 Samoa tsunami around Tutuila, American Samoa. *Geophysical Research Letters*, 37(21). https://doi.org/10.1029/2010GL044419
  - Salcedo, J. C., & Hara, T. (2011). Earthquake source parameters for subduction zone events causing tsunamis in and around the Philippines. *Bulletin of the International Institute of Seismology and Earthquake Engineering*, 45, 49–54.
  - Satake, K. (2002). 28 Tsunamis. In W. H. K. Lee, H. Kanamori, P. C. Jennings, & C. Kisslinger (Eds.), *International Handbook of Earthquake and Engineering Seismology, Part A* (pp. 437–451). Academic Press. https://doi.org/10.1016/S0074-6142(02)80231-5
  - Satake, K. (2023). Recurrence and Long-Term Evaluation of Kanto Earthquakes. *Bulletin of the Seismological Society of America*, 113(5), 1826–1841. https://doi.org/10.1785/0120230072
  - Schambach, L., Grilli, S. T., Tappin, D. R., Gangemi, M. D., & Barbaro, G. (2020). New simulations and understanding of the 1908 Messina tsunami for a dual seismic and deep submarine mass failure source. *Marine Geology*, 421(December 2019), 106093. https://doi.org/10.1016/j.margeo.2019.106093
- Schellart, W. P., & Rawlinson, N. (2013). Global correlations between maximum magnitudes of subduction zone interface thrust earthquakes and physical parameters of subduction zones. *Physics of the Earth and Planetary Interiors*, 225, 41–67. https://doi.org/10.1016/j.pepi.2013.10.001
  - Simons, W. J. F., Ambrosius, B. A. C., Noomen, R., Angermann, D., Wilson, P., Becker, M., Reinhart, E., Walpersdorf, A., & Vigny, C. (1999). Observing plate motions in S.E. Asia: Geodetic results of the GEODYSSEA Project. *Geophysical Research Letters*, 26(14), 2081–2084. https://doi.org/10.1029/1999GL900395
- 585 Storchak, D. A., Di Giacomo, D., Bondar, I., Engdahl, E. R., Harris, J., Lee, W. H. K., Villasenor, A., & Bormann, P. (2013). Public Release of the ISC-GEM Global Instrumental Earthquake Catalogue (1900-2009). Seismological Research Letters, 84(5), 810–815. https://doi.org/10.1785/0220130034
  - Storchak, D. A., Di Giacomo, D., Engdahl, E. R., Harris, J., Bondár, I., Lee, W. H. K., Bormann, P., & Villaseñor, A. (2015). The ISC-GEM Global Instrumental Earthquake Catalogue (1900–2009): Introduction. *Physics of the Earth and Planetary Interiors*, 239, 48–63. https://doi.org/10.1016/j.pepi.2014.06.009
  - Stratta, J. L., Canon, T. J., Duke, M. C., & Selna, L. G. (1977). *Reconnaissance Report of the Mindanao, Philippine Earthquake of August 17, 1976.* https://nehrpsearch.nist.gov/static/files/NSF/PB290351.pdf#page=21.09
  - Straume, E. O., Gaina, C., Medvedev, S., Hochmuth, K., Gohl, K., Whittaker, J. M., Abdul Fattah, R., Doornenbal, J. C., & Hopper, J. R. (2019). GlobSed: Updated Total Sediment Thickness in the World's Oceans. *Geochemistry, Geophysics, Geosystems*, 20(4), 1756–1772. https://doi.org/10.1029/2018GC008115
  - Strusińska-Correia, A. (2017). Tsunami mitigation in Japan after the 2011 Tōhoku Tsunami. *International Journal of Disaster Risk Reduction*, 22, 397–411. https://doi.org/10.1016/j.ijdrr.2017.02.001
  - Suppasri, A., Muhari, A., Ranasinghe, P., Mas, E., Shuto, N., Imamura, F., & Koshimura, S. (2012). Damage and reconstruction after the 2004 Indian Ocean tsunami and the 2011 Great East Japan tsunami. *Journal of Natural Disaster Science*, 34(1), 19–39. https://doi.org/10.2328/jnds.34.19
  - Takagi, H., Pratama, M. B., Kurobe, S., Esteban, M., Aránguiz, R., & Ke, B. (2019). Analysis of generation and arrival time of landslide tsunami to Palu City due to the 2018 Sulawesi earthquake. *Landslides*, *March*, 983–991. https://doi.org/10.1007/s10346-019-01166-y
- Vela, J., Pérez, B., González, M., Otero, L., Olabarrieta, M., Canals, M., & Casamor, J. L. (2014). Tsunami Resonance in Palma Bay and Harbor, Majorca Island, as Induced by the 2003 Western Mediterranean Earthquake. *The Journal of Geology*, 122(2), 165–182. https://doi.org/10.1086/675256
  - Wu, T.-R., & Huang, H.-C. (2009). Modeling tsunami hazards from Manila trench to Taiwan. *Journal of Asian Earth Sciences*, 36(1), 21–28. https://doi.org/10.1016/j.jseaes.2008.12.006
  - Yamazaki, Y., & Cheung, K. F. (2011). Shelf resonance and impact of near-field tsunami generated by the 2010 Chile earthquake. *Geophysical Research Letters*, 38(12), n/a-n/a. https://doi.org/10.1029/2011GL047508
  - Yumul, G. P., Dimalanta, C. B., Maglambayarw, V. B., & Marquez, E. J. (2008). Tectonic setting of a composite terrane: A review of the Philippine island arc system. *Geosciences Journal*, 12(1), 7–17. https://doi.org/10.1007/s12303-008-0002-0
  - Yumul, G. P., Dimalanta, C. B., Tamayo, R. A., & Maury, R. C. (2003). Collision, subduction and accretion events in the



620



- 615 Philippines: A synthesis. *Island Arc*, *12*(2), 77–91. https://doi.org/10.1046/j.1440-1738.2003.00382.x Zahirovic, S., Seton, M., & Müller, R. D. (2014). The Cretaceous and Cenozoic tectonic evolution of Southeast Asia. *Solid Earth*, *5*(1), 227–273. https://doi.org/10.5194/se-5-227-2014
  - Zhao, G., & Niu, X. (2022). Local amplification of tsunami waves along the west coast of Negros Island and Panay Island. *Applied Ocean Research*, 123(July 2021), 103175. https://doi.org/10.1016/j.apor.2022.103175